Ultra-wideband Millimeter-wave Antenna Arrays and Front-end Systems

For high data rate 5G and high energy physics applications

IMRAN AZIZ

Dissertation presented at Uppsala University to be publicly examined in Polhemsalen, Ångströmlaboratoriet, Lägerhyddsvägen 1, Uppsala, Monday, 15 March 2021 at 09:15 for the degree of Doctor of Philosophy. The examination will be conducted in English. Faculty examiner: Associate Professor Ville Viikari (Aalto University, Finland).

Abstract
Aziz, I. 2021. Ultra-wideband Millimeter-wave Antenna Arrays and Front-end Systems. For high data rate 5G and high energy physics applications. *Digital Comprehensive Summaries of Uppsala Dissertations from the Faculty of Science and Technology* 2005. 68 pp. Uppsala: Acta Universitatis Upsaliensis. ISBN 978-91-513-1122-7.

The demand for wireless data communications is rapidly increasing due to several factors including increased internet access, increasingly growing number of mobile users and services, implementation of the Internet of Things (IoT), high-definition (HD) video streaming and video calling. To meet the bandwidth requirement of new and emerging applications, it is necessary to move from the existing microwave bands towards millimeter-wave bands.

This thesis presents different antenna arrays at 60 GHz and 28 GHz that are integrated with the front-end RFIC to steer the beam in ≈ ±50° in the azimuth plane. The 5G antenna arrays at 28 GHz are designed to provide broadband high data rate services to the end users. In order to transport this high-volume data to the core network, a fixed wireless access (FWA) link demands the implementation of a broadband, high gain and steerable narrow-beam array. The 60 GHz antenna arrays, presented in this thesis, are good candidates for both FWA as well as backhaul communications. The two proposed arrays at 60 GHz (57-66 GHz) are i) a stacked patches array and ii) a connected slots array feeding a high gain lens antenna. The 2×16 stacked patches antenna array shows more than 20 dBi realized gain. The array is integrated with the front-end RFIC and the resulting module shows > 40 dBm measured effective isotropic radiated power (EIRP). The other 60 GHz antenna array is designed as linear connected slots with sixteen equidistant feeding points. The latest is then used as a feeder of a high gain dielectric lens. Peak measured gain of 25.4 dBi is achieved with this antenna. Moreover, instead of experiencing scan loss, the lens is designed to get higher gain when the beam is steered away from the broadside direction.

Furthermore, two compact antenna arrays are designed at 28 GHz (24.25 - 29.50 GHz). A linear polarized (LP) and a circular polarized (CP) array are realized in the fan-out embedded wafer level ball-grid-array (eWLB) package. In comparison with the PCB arrays, this antenna in package (AiP) solution is not only cost-effective but it also reduces the integration losses because of shorter feed lines and no geometrical discontinuity. The LP array is realized as a dipole antenna array feeding a novel horn-shaped heatsink. The RF module gives 34 dBm peak EIRP with beam-steering in ±35°. Besides, the CP antenna array is realized with the help of crossed dipoles and the RF module provides 31 dBm peak EIRP with beam-steering in ±50°.

The data demands are not limited to the telecom industry as the upgradation of accelerators and experiments at the large hadron collider (LHC) at CERN will result in increased event rate thus demanding higher data rate front-end readout systems. This work thus investigates the feasibility of 60 GHz wireless links for the data readout at CERN. For this purpose, the 60 GHz wireless chips are irradiated with 17 MeV protons [dose 7.4 Mrad (RX) & 4.2 Mrad (TX)] and 200 MeV electrons [dose 270 Mrad (RX) & 314 Mrad (TX)] in different episodes. The chips have been found operational in the post-irradiation investigations with some performance degradation. The encouraging results motivate to move forward and investigate the realization of wireless links in such a complex environment.

Imran Aziz, Department of Electrical Engineering, Solid-State Electronics, Box 534, Uppsala University, SE-751 21 Uppsala, Sweden.

*Dedicated to the peace of my heart, my daughter, **Amna Aziz,***
with her birth this journey started
*And to my sweet son, **Hamza Aziz,***
with whose birth this journey is gonna end.

List of papers

This thesis is based on the following papers, which are referred to in the text by their Roman numerals.

I **I. Aziz**, R. Dahlbäck, E. Öjefors, K. Sjögren, A. Rydberg and D. Dancila, **60 GHz compact broadband antenna arrays with wide-angle beam steering**, in The Journal of Engineering, vol. 2019, no. 8, pp. 5407–5414, 8 2019, doi: 10.1049/joe.2018.5343.

II **I. Aziz**, D. Dancila, S. Dittmeier, A. Siligaris, C. Dehos, P. Lurgio, Z. Djurcic, G. Drake, J. Jimenez, L. Gustaffson, D. Kim, E. Locci, U. Pfeiffer, P. Vazquez, D. Röhrich, A. Schöning, H. Soltveit, K. Ullaland, P. Vincent, S. Yang and R. Brenner, **Effects of proton irradiation on 60 GHz CMOS transceiver chip for multi-Gbps communication in high-energy physics experiments**, in The Journal of Engineering, vol. 2019, no. 8, pp. 5391–5396, 8 2019, doi: 10.1049/joe.2018.5402.

III **I. Aziz**, E. Öjefors and D. Dancila, **Connected Slots Antenna Array Feeding the High Gain Lens for Wide-angle Beam-steering Applications**, Accepted for publication in International Journal of Microwave and Wireless Technologies (IJMWT).

IV **I. Aziz**, B. Franzen, E. Öjefors and D. Dancila, **Broadband beam-steerable WiGig module for high data rate access and backhaul communications**, Manuscript submitted for publication.

V **I. Aziz**, D. Wu, E. Öjefors, J. Hannings, E. Wiklund and D. Dancila, **28 GHz Compact Dipole Antenna Array Integrated in Fan-out eWLB Package**, Manuscript submitted for publication.

VI **I. Aziz**, J. Hannings, E. Öjefors, D. Wu, E. Wiklund and D. Dancila, **28 GHz Circular Polarized Fan-out Antenna Array with Wide-angle Beam-steering**, Manuscript.

Reprints were made with permission from the publishers.

Other publications

Following papers are not included in this thesis because of either overlap or the contents are outside the scope of this thesis.

I   **I. Aziz**, R. Dahlbäck, E. Öjefors, A. Rydberg and D. Dancila, **High gain compact 57 – 66 GHz antenna array for backhaul & access communications**, 12th European Conference on Antennas and Propagation (EuCAP 2018), London, 2018, pp. 1–4, doi: 10.1049/cp.2018.0362.

II   **I. Aziz**, A Rydberg and D Dancila, **Electromagnetically Coupled Multi-layer Patch Antenna for 60 GHz Communications**, GigaHertz Symposium, Lund, May 24–25, 2018.

III   **I. Aziz**, E. Öjefors, R. Dahlbäck, A. Rydberg, G. Engblom and D. Dancila, **Broadband Connected Slots Phased Array Feeding a High Gain Lens Antenna at 60 GHz**, 2019 49th European Microwave Conference (EuMC), Paris, France, 2019, pp. 718–721,
doi: 10.23919/EuMC.2019.8910856.

IV   **I. Aziz** on behalf of WADAPT collaboration, **Proton Irradiation Hardness Investigations of 60 GHz Transceiver Chips for High Energy Physics Experimentations**, poster presented at VCI2019 - The 15th Vienna conference on instrumentation, 18–22 Feb, 2019.
URL: https://indico.cern.ch/event/716539/contributions/3256662/

V   **I. Aziz**, W. Liao, H. Aliakbari and W. Simon, **Compact and Low Cost Linear Antenna Array for Millimeter Wave Automotive Radar Applications**, 2020 14th European Conference on Antennas and Propagation (EuCAP 2020), Copenhagen, Denmark, 2020, pp. 1–4,
doi: 10.23919/EuCAP48036.2020.9135772.

VI   **I. Aziz**, D. Wu, E. Öjefors, J. Hanning, E. Wiklund and D. Dancila, **Broadband fan-out phased antenna array at 28 GHz for 5G applications**, Accepted for EuMW2020.

VII   E. Öjefors, D. Dancila, **I. Aziz**, J. Hanning, **Arrangement comprising an integrated circuit package and a heatsink element**, Patent application filed, application number EP21150555.7, Jan 2021.

VIII   E. Öjefors, D. Dancila, **I. Aziz**, J. Hanning, **Arrangement comprising crossed dipole array integrated in the package**, Patent application in process.

Contents

1. Introduction

1.1 Motivation

Internet data demand is rapidly increasing globally due to a number of factors including increased internet access, grown number of mobile phone users and services, realization of Internet of Things (IoT), high-definition (HD) video streaming, video calling etc. [1–3]. This increase in the demand is directly linked with the technology enhancement that can assure the availability of above mentioned services. As most of the services ask for immediate wireless data, it is very challenging to meet these requirements without considering additional high frequency bands, apart from the saturated sub-6 GHz bands [4].

1.1.1 Millimeter-wave frequency bands

The license-free 60 GHz band (57–66 GHz) is one of the most suitable and available options, which can help to cope with such high data demands. WiGig, also known as 60 GHz WiFi, is meant for different services like audio/video data transmission, display interfaces for HDTVs/monitors/projectors, wireless local area networking (WLAN), fixed wireless access (FWA) and backhaul communications etc. As shown in Fig. 1.1, the 57–66 GHz bandwidth is divided into 4 channels where each channel has a bandwidth of 2.16 GHz. The 802.11ad standard defines the 60 GHz WLAN standard which not only supports up to 8 Gbps throughput but also ensures the seamless transition between the existing WiFi bands (2.4 GHz and 5 GHz) and 60 GHz band [5].

Moreover, as shown in Fig. 1.2, the 3rd generation partnership project (3GPP) has specified n258 (24.25 – 27.50 GHz) and n257 (26.50 – 29.50 GHz) frequency bands for 5G communications. These bands, which are also called 26 GHz and 28 GHz respectively, intend to provide high data rate services for
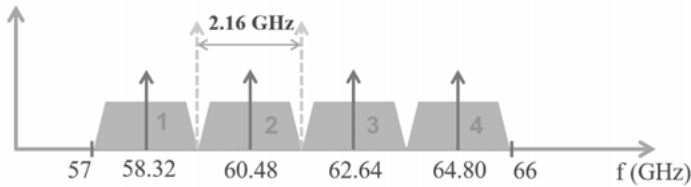

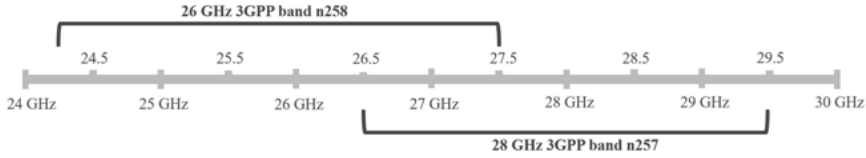Fig. 1.1. Four 60 GHz channels each of 2.16 GHz bandwidth.

Fig. 1.2. Frequency bands 26 GHz (n258) and 28 GHz (n257).

short distances in high user density area, such as train/metro stations, densely populated areas, city centers, gathering places etc. Besides, homes and businesses with FWA, IoT, 4K and 8K video streaming, industrial automation with low latency and high reliability are some other potential applications [6].

1.1.2 Millimeter-wave links for tracker data read-out at CERN

The upgrade of accelerators and experiments at the Large Hadron Collider (LHC) for high luminosity will result in multiple times higher event (collision) rates, which demands high data rate readout systems [7]. For instance, the readout data requirements at the upgraded ATLAS silicon microstrip tracker will be from 50 to 100 Tbps [8,9]. The availability of unlicensed 9 GHz bandwidth at 60 GHz (57–66 GHz) can fulfil this demand, as a single link can achieve multi-Gbps. However, wireless data transmission using millimeter-wave technology has not yet been used in trackers for particle physics experiments. The Wireless Allowing Data and Power Transmission (WADAPT) proposal [10] was formed to study the feasibility of wireless technologies in High Energy Physics (HEP) experiments at the European organization for nuclear research (CERN). The objective is to provide a common platform for research and development in order to optimize the effectiveness and cost, with the aim of designing and testing wireless demonstrators for large instrumentation systems.

A strong motivation for using wireless data transmission is the absence of wires and connectors which will be an advantage in areas with low material budget and will also reduce the passive material. This passive material degrades the tracker performance through scattering and particle conversion. Besides, wireless transmission allows radial readout through the layers shown in Fig. 1.3 (a) which opens for topological readout of tracking data instead of current axial wired links shown in Fig. 1.3 (b). This topological readout of the tracking data can also reduce the on-detector data volume using inter-layer communications, and will drastically reduce the readout time and latency [12].

1.1.3 Beam-steering

High gain antennas and antenna arrays are required to achieve high throughput, which results in a narrow beam coverage, as beamwidth is inversely pro-
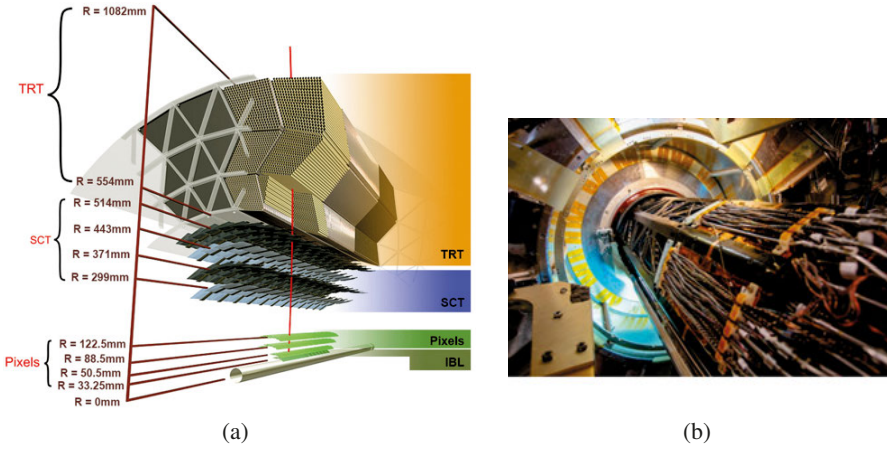
Fig. 1.3. ATLAS inner detectors [11] (a) Layered view of inner detectors (b) Pixel detector showing significant cables contribution in active detector volume.

portional to the gain of an antenna array. In order to increase the coverage and provide point-to-multipoint high data rate connectivity, beam-steering is essential at millimeter-wave bands. The front-end system can provide specific weights (phases and amplitudes) to the individual antenna elements in the array to steer the beam in a desired direction. As shown in Fig. 1.4, beam-steering focuses the electromagnetic power towards specific targets instead of having the waves spread in all directions. This improves the spectral efficiency (bit/s/Hz) through higher signal-to-noise ratio (SNR) which results in achieving higher data rates. Beam-steering also helps to overcome the interference caused by obstacles during the transmission in real-time. Concerning backhaul communications, beam-steering diminishes the need of having separate antennas for every link through high capacity point-to-multipoint connectivity. For wireless data readout at CERN, there will be thousands of closely spaced wireless links where beam-steering can enhance communication robustness through point-to-multipoint connectivity.

1.2 Thesis Objective

In this thesis, different broadband and high gain millimeter-wave antenna arrays are realized to fulfil the data demands in different application scenarios. The arrays are integrated with the front-end radio frequency integrated circuits (RFIC) to steer the beam in a desired directions. The 5G antenna arrays at 28 GHz are designed for places with high user density as well as for customer premises equipment (CPE) applications. To transport this high volume data to the core network, a fixed wireless access (FWA) link demands the implementation of a broadband, high gain and steerable narrow-beam array. This thesis
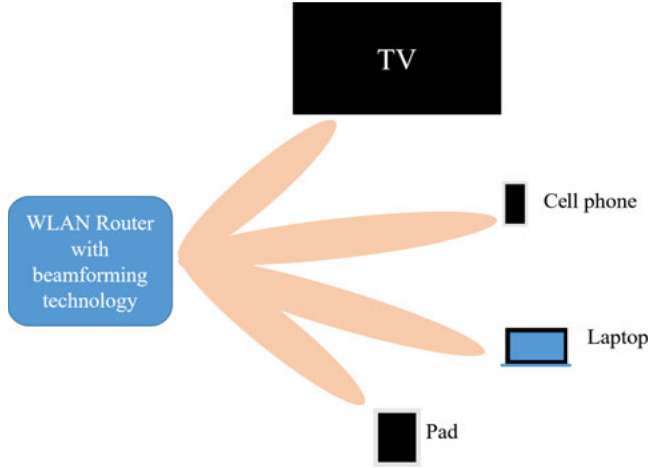
Fig. 1.4. High throughput connectivity with multiple devices through beam-steering.

presents the 60 GHz antenna arrays that satisfy these conditions and they can be used for both FWA as well as backhaul communications.

At 60 GHz, a printed circuit board (PCB) antenna array integrated with the front-end RFIC is presented in **Paper I and IV**, whereas a broadband connected slots array feeding a high gain lens is designed in **Paper III**. To address the end user high data rate requirements, two antenna arrays are realized at 28 GHz. Instead of using a low-loss RF PCB, **Paper V** and **Paper VI** present the compact phased antenna arrays realized in the fan-out embedded wafer level ball grid array (eWLB) package. In comparison with the PCB antenna arrays, this antenna in package (AiP) solution is not only cost effective but it also reduces the interconnection losses.

Moreover, for high data rate readout links at CERN, the key requirement are the components that can tolerate this radiation hard environment. As a first step towards this realization, a 17 MeV proton irradiation experiment is carried out at Åbu, Finland and **Paper II** presents the irradiation effects on a 60 GHz front-end transceiver chip. Besides, this thesis also presents a 200 MeV electron irradiation of the chip, performed at CLEAR, CERN.

1.3 Thesis Organization

The thesis is organized as follows: Chapter 2 discusses the wave propagation along with losses and challenges for different environments. Chapter 3 presents individual elements used as building blocks for different arrays presented in Chapter 4. The measurement methods used in this doctoral thesis are presented in Chapter 5, while Chapter 6 discusses the the beam-steering radiation pattern results. And at the end, proton and electron irradiation effects on the 60 GHz front-end transceiver chip are briefly discussed in Chapter 7.

2. Wave Propagation

The availability of larger bandwidths at millimeter-waves comes with the challenges like increased free space path loss, higher atmospheric absorption, scattering, etc. These factors are further discussed in this chapter.

2.1 Free Space Propagation

The free space path loss is the major loss factor in mm-wave propagation. For electromagnetic waves propagating in free space, the power received by an antenna reduces four times (6 dB) as the distance between transmitting and receiving antennas is doubled. For two isotropic antennas, wavelength and distance dependence on the loss is given by the relation [13]:

$$L_{\text{free space}} = (4\pi R/\lambda)^2 \tag{2.1}$$

For loss in dBs:

$$L_{\text{free space}}(\text{dB}) = 20 \log_{10}(4\pi R/\lambda) \tag{2.2}$$

where R is the line of sight (LOS) distance between two antennas and λ is the free space wavelength at the operating frequency. As an example, the free space path loss at 1 m distance for a 60 GHz link is 68 dB and for 5 GHz it is 46 dB. It is worth mentioning that this example is only true if the electrical size of the antennas (in terms of wavelength) is same for both 60 GHz and 5 GHz links, i.e., the free space path loss does not change with the frequency if the physical area of the antenna remains constant [14]. The Friis transmission equation gives more detailed relation by taking into account other transmit and receive factors [15].

$$P_{\text{r}} = P_{\text{t}} \, G_{\text{r}} \, G_{\text{t}} \, \frac{\lambda^2}{(4\pi R)^2} \tag{2.3}$$

where P_{r} and P_{t} are received and transmitted powers while G_{r} and G_{t} are gains of receive and transmit antennas, respectively.

2.2 Atmospheric and Other Losses

Apart from the free space loss, there are also other factors which affect the microwave and millimeter-wave propagation. Some of these factors are gases in

the atmosphere, rain, hydrometeors and micrometeors which not only absorb the electromagnetic energy but also cause the waves to scatter in un-desired directions. It can be Rayleigh scattering which occurs if the particles' diameter is less than about one-tenth of propagating wavelength, or Mie scattering when particle diameter is larger than the wavelength [16]. The attenuation of electromagnetic energy due to absorption by water vapours and oxygen is presented in Fig. 2.1 [17]. For frequencies below 100 GHz, water vapour absorption has a peak at 24 GHz while attenuation due to oxygen absorption is 10-15 dB/km around 60 GHz.

Besides, the loss due to reflection and diffraction mainly depends upon the material and the surface on which the waves strike. On one hand, reflection and diffraction reduce the propagation range of millimeter-waves, but on the other hand, these factors also facilitate non-line-of-sight (NLOS) communication [14].
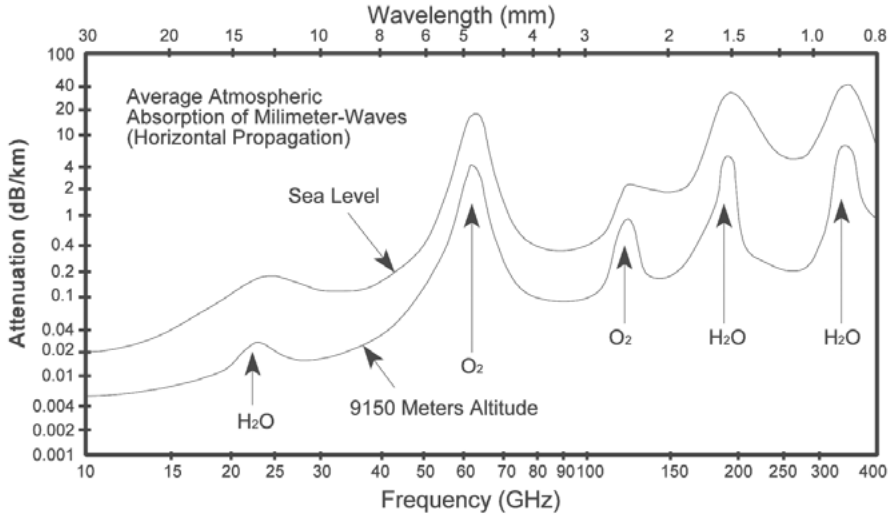
Fig. 2.1. Attenuation at mm-wave due to water vapours and oxygen absorptions.

2.3 Wave Propagation in Trackers at CERN

The trackers at CERN are flushed with dry nitrogen (N_2), hence oxygen absorption of 60 GHz waves is not a problem for high energy physics applications. Besides, higher attenuation at 60 GHz allows for spatial frequency re-use in more compact regions. This makes 60 GHz a good candidate for inter-layer communications at CERN detectors, as the link distances are in tens of centimeters. Fig. 2.2 shows the proposed wireless links on the trackers to replace the existing wired connections. It can be realized that even if

Fig. 2.2. Proposed 60 GHz wireless links for total/partial replacement of cables. The green lines are silicon detector modules placed on co-axial cylindrical layers.

the cross-talk between layers is expected to be small, the interference between links on the same layer can be a challenge. This effect can probably be moderated by using high gain directional antennas and utilizing absorbing materials between links, besides studies have shown that antennas can be placed as close as 10 cm apart [8]. By exploiting polarization, the density of the links can be further increased.

3. Antenna Elements: Building Blocks for Phased Arrays

This chapter presents different antenna elements, e.g., microstrip patch antenna, dipole antenna and slot antenna, which are further used for designing antenna arrays for beam-steering applications. One common factor between above mentioned elements is their planarity which provides ease of integration with front-end radio frequency integrated circuit (RFIC).

3.1 Microstrip Patch Antenna

First introduction of microstrip patch antennas can be traced back to 1950's [18] though it gained more attention in 1970's after the development of printed circuit board (PCB) technology. The microstrip patch antenna is a very common type of antennas and is used for a wide variety of applications because of their advantages: compactness, planar configuration, cost effectiveness, simple fabrication and ease of integration with RFIC. However, they are low gain antennas and inherently narrow banded, as their length (L) determines the resonance frequency (see Fig. 3.1). The impedance bandwidth of the patch antenna can be increased by using a thick substrate, but this gives rise to increased surface waves inside the substrate and thus more losses. The power coupled to these surface waves not only results in reduced radiation efficiency of the antenna but also increases the mutual coupling between elements in an antenna array. Another method to increase the bandwidth is by using low relative permittivity (ε_r) substrates. This can be explained by the fact that increasing ε_r reduces the size of element (as 'L' depends upon ε_r) which in turn increases the quality factor (Q) of the resonator, thus making it more narrowband [19].

For millimeter-wave applications, another challenge namely fabrication tolerances become very important. As all the design dimensions are directly proportional to the wavelength, thus the lengths and widths reduce significantly at millimeter-waves frequencies. The widths of the feed transmission lines typically become very thin, around 1/10th of a millimeter, imposing serious fabrication tolerances and thus the fabrication cost can rise significantly as such tolerances can only be met with more expensive fabrication equipment.

Different methods like transmission line model, cavity model or full-wave analysis [20–23] can be used to analyse the microstrip patch antennas. Based

on the transmission-line model, a set of design guidelines are outlined in this section. These guidelines can lead to a first iteration of the patch element that can be further optimized [24, 25].

(a)

(b)

(c)
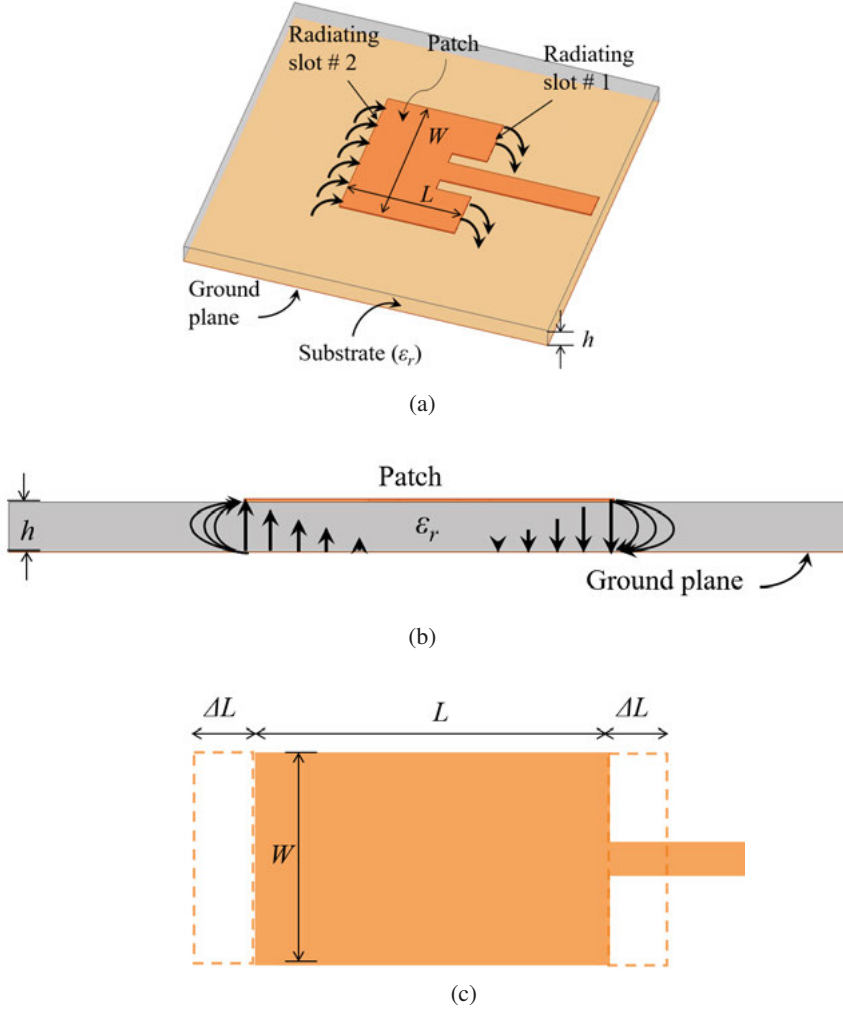
Fig. 3.1. Microstrip patch antenna (a) overall view (b) cross-sectional view of the patch showing the fringing fields (c) effective length of the patch extended along radiating edges.

3.1.1 Design principles

As shown in the Fig. 3.1 (a), a microstrip patch antenna has two radiating edges acting as radiating slots. The resonant frequency of the microstrip patch antenna depends upon its length L and the relation for the dominant mode TM_{010} is given by

$$f = \frac{c}{2L\sqrt{\varepsilon_r}} \tag{3.1}$$

where c is the speed of light in free space and ε_r is the relative permittivity of the substrate.

Looking at the cross-sectional view in Fig. 3.1 (b), the fields extend away from the edges of the patch, called fringing fields, which is the function of L/h (h is the height of substrate) and ε_r. Moreover, the fields are not completely confined within the substrate but some lines also exist in the air (in case of dielectric-air interfaces). As the waves are present both in substrate and air, an effective dielectric constant (ε_{reff}) is introduced to account for fringing and make the medium look homogeneous. Value of ε_{reff} can be anywhere between 1 and ε_r depending upon the relative permittivity of the substrate and W/h ratio.

$$\varepsilon_{reff} = \frac{\varepsilon_r + 1}{2} + \frac{\varepsilon_r - 1}{2}[1 + 12\frac{h}{W}]^{-1/2} \tag{3.2}$$

where W is the width of the patch. As both L and W are unknown at this stage, one can begin by using the below relation for width

$$W = \frac{c}{2f}\sqrt{\frac{2}{\varepsilon_r + 1}} \tag{3.3}$$

Because of the fringing fields, effective length L_{eff} of the patch is somewhat larger than the physical length L as shown in Fig. 3.1 (c),

$$L_{eff} = L + 2\Delta L \tag{3.4}$$

where ΔL can be calculated using the equation below:

$$\Delta L = 0.412h\frac{(\varepsilon_{reff} + 0.3)(W/h + 0.264)}{(\varepsilon_{reff} - 0.258)(W/h + 0.8)} \tag{3.5}$$

Including the above mentioned fringing field effects in Eq. 3.1, it will become

$$f = \frac{c}{2L_{eff}\sqrt{\varepsilon_{reff}}} \tag{3.6}$$

The actual length of the patch can then be determined by evaluating

$$L = \frac{c}{2f\sqrt{\varepsilon_{reff}}} - 2\Delta L \tag{3.7}$$

As mentioned earlier, the above equations shall give approximate dimensions, which can then be optimized using electromagnetic simulation softwares.

3.2 Stacked Patches Antenna

Another method to increase the bandwidth of a narrow-band patch antenna is to introduce more than one closely spaced resonant structures. The electromagnetic coupling between stacked multi-layer patches shows a broadband impedance bandwidth and increased gain performance of the patch antenna [26–29]. This antenna can be designed using a stacked patch structure where one patch can be fed through probe or microstrip line while the other patch is electromagnetically coupled. The closely spaced resonances make the antenna broadband. The patches can be of rectangular or circular shapes. Fig. 3.2 (a) and (b) shows a stacked patches structure where the rectangular patch is fed through a microstrip line on M2 metallic layer while the circular patch is placed on M1 layer.
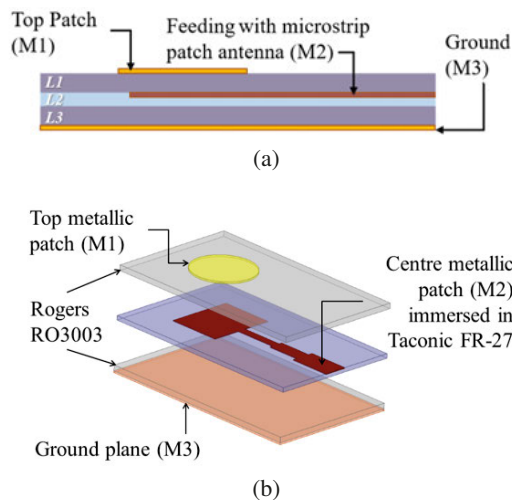

(a)

(b)

Fig. 3.2. Different views of stacked patches where rectangular patch is fed through microstrip line and circular patch is fed through proximity effects. (a) Cross-sectional view. (b) Layered view.

The stacked patches structure is defined by a number of dimensions, like height of the substrates, lengths, widths and diameters of bottom and top patches. These dimensions can be varied to get optimized values. Fig. 3.3 shows reflection coefficient (S11) graph for different parasitic patch diameter (ppd) values of the top circular patch, while keeping the other dimensions constant. The two resonances are very obvious in the graphs. These closely spaced resonances result in the < -10 dB impedance bandwidth of more than 20 %. Similar results are obtained when length of the rectangular patch on the bottom is varied. These stacked elements are used to design different series and parallel antenna arrays which are further discussed in the next chapter.
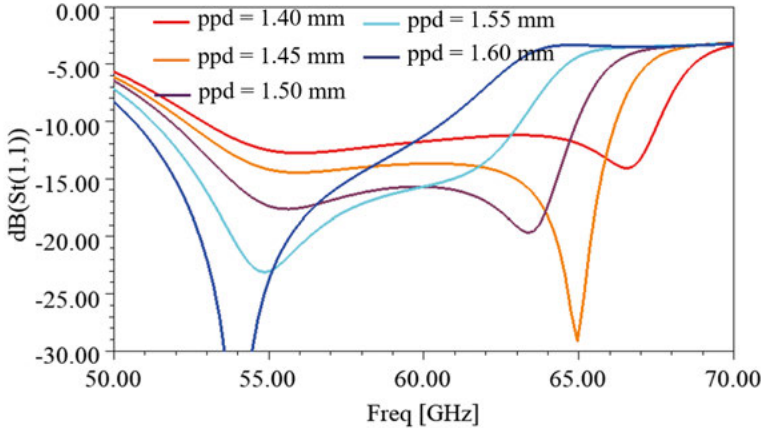
Fig. 3.3. S11 for different values of the parasitic patch diameter (ppd).

3.3 Dipole Antenna

Dipole antenna is a widely used antenna which most commonly consists of two quarter-wave long legs as shown in Fig. 3.4 (a). The current (blue curve) is zero while voltage (red curve) is maximum at the edges for a half wave long dipole.

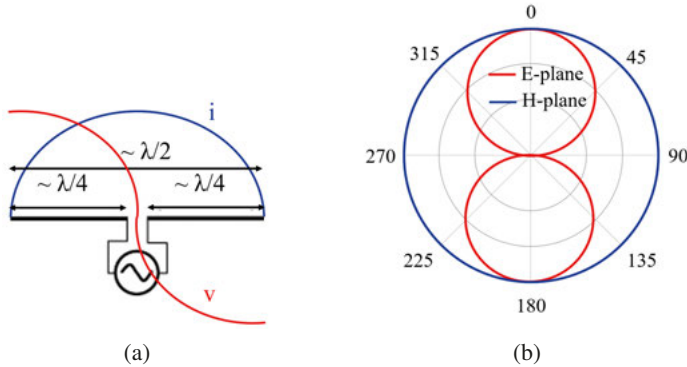(a)   (b)

Fig. 3.4. (a) A half wave dipole antenna consisting of two quarter wavelength long legs. (b) E- and H-plane radiation pattern of the dipole.

The input impedance of the dipole is real when the dipole length is close to half wavelength, which makes it a resonant antenna. This antenna can be realized with the help of wires, metallic rods or metallic patches on the PCB. Besides, unlike a patch antenna, the dipole antenna does not require a ground plane as both of its legs are fed 180° out of phase. Fig. 3.4 (b) shows the E- and H-plane radiation pattern for a half-wave dipole antenna. The radiation is omni-directional in the H-plane and has two lobes in the E-plane. In 3D, this pattern looks like a doughnut.

3.4 Slot Antenna

Slot antenna is a type of aperture antenna where an opening is made in a metallic sheet. The energy radiates when a high frequency field exists on the conducting plane around a narrow slot. According to Babinet's principle, a slot antenna is a complementary structure to a dipole antenna as shown in Fig. 3.5. This means that the polarization, current and voltage distribution around the slot are complementary to that of the dipole antenna. As an example, if a dipole antenna is placed vertically, it will have vertical polarization while if a slot antenna is placed vertically it will have horizontal polarization. Besides, the radiation pattern for a slot antenna is similar to that of a dipole antenna.
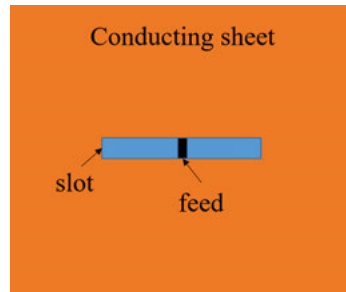

Fig. 3.5. A half wave slot antenna fed in the center.

4. Antenna Arrays for Beam-steering Applications

This chapter briefly explains the design and fabrication of different antenna arrays presented in the thesis. Before proceeding to the design of antenna arrays, it is important to have a look at the array factor, which explains how arrays behave compared to a single stand-alone element.

4.1 Array Factor

The antenna elements are placed at a specific distance from each other to create an antenna array. Each element can be fed in a way to direct the antenna array towards a specific direction. The proper selection of weights (amplitude and phase) to the individual elements in the array can increase the energy in one direction while canceling out the signals from undesired directions. The combination of antenna element radiation pattern and its position in the antenna array defines the array factor. As the name suggests, the array factor has great importance in the array theory.
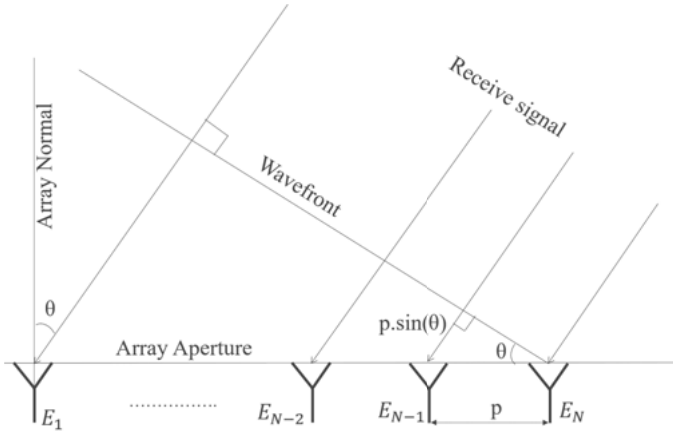

Fig. 4.1. A linear array having equally spaced N number of elements and with a signal is being received at an angle θ to the array normal.

A linear phased array is shown in Fig. 4.1 where the elements are spaced by a distance p from each other with a plane wave received at an angle θ with respect to the array normal. Due to the reciprocity theorem, the same

results apply for the transmit mode. As the wave can have both time and space dependence, the phase is expressed as

$$\phi = \omega t \pm \frac{2\pi}{\lambda} l = \omega t \pm kl \qquad (4.1)$$

where $k = \frac{2\pi}{\lambda}$ is the wave number. The received signal will travel a distance $p\sin\theta$ from the element number N to element $N-1$, and likewise $2p\sin\theta$ to $N-2$. If we neglect the time dependence term in the receive signal, phase of the signal received by the ith element will be

$$\phi_i = k_0(N-i)\ p\ \sin\theta \qquad (4.2)$$

for $i = 1, 2, ..., N-1,\ N$ and where k_0 is the free space wave number.

If $R_e(\theta)$ is the radiation pattern of individual element, then the signal received by the ith element will be

$$R_i(\theta) = R_e(\theta)\ A_i\ e^{jk_0(N-i)\ p\ \sin\theta} \qquad (4.3)$$

where A_i is the amplitude of the signal received by ith element. Then the total power received by the array can be written as a summation:

$$R(\theta) = \sum_{i=1}^{N} R_i(\theta) \qquad (4.4)$$

expansion gives

$$R(\theta) = R_e(\theta) \sum_{i=1}^{N} A_i\ e^{jk_0(N-i)\ p\ \sin\theta} \qquad (4.5)$$

Thus, the total radiation pattern of an antenna array is the *pattern multiplication* of two terms, individual element pattern $[R_e(\theta)]$ and a summation term. This multiplication tells that in order for an array to have a wide-angle beam-steering, the individual element should have a wide beam radiation pattern [30–34]. The summation term in Eq. 4.5 is called the array factor and is defined as the radiation pattern of an array having N isotropic elements [35].

$$\text{Array Factor} = \text{AF} = \sum_{i=1}^{N} A_i\ e^{jk_0(N-i)\ p\ \sin\theta} \qquad (4.6)$$

The array factor is thus the function of weights to the individual elements and spacing between them.

4.2 Stacked Patches Antenna Array

This section briefly discusses the design of the stacked microstrip antenna array presented in paper I. The aim is to design an array having less than -10 dB

impedance bandwidth as well as the 3 dB gain bandwidth covering the complete 60 GHz license free band 57–66 GHz with wide-angle beam-steering. Moreover, the array needs to be compact and planar as it will be integrated with a front-end radio frequency integrated circuit (RFIC) [36]. Keeping above mentioned requirements in view, the microstrip patch antenna elements are selected after investigating different antenna elements. A choice is made based on their compactness and ease of integration with the RFIC. Besides, wide beamwidth of the patch antenna can help to achieve wide-angle beam-steering [37]. This antenna however lacks in impedance bandwidth because of its resonant structure. As discussed in Section 3.2, this limitation is overcome by using stacked patches which improves the impedance bandwidth. Different multi-layer structures working at 60 GHz are realized using low temperature co-fired ceramics (LTCC) [38–41]. The LTCC provides flexibility in realizing arbitrary number of layers, cross layer VIAs and open and embedded cavities. However, it has a disadvantage of relatively higher cost compared with a printed circuit board (PCB) process [42]. The PCB implementation has been used in [29] to realize 5-metal layers differential phased array antenna at 60 GHz. Likewise, a 4-metal layers, microstrip line fed, aperture coupled multi-layer antenna array is presented in [43]. In the present work, we have used 3-metal layers (one ground layer and two layers with stacked patches) to design the antenna array, besides, a low ε_r material is used in the design as high ε_r increases the Q factor and makes the patch more narrow-band [19].
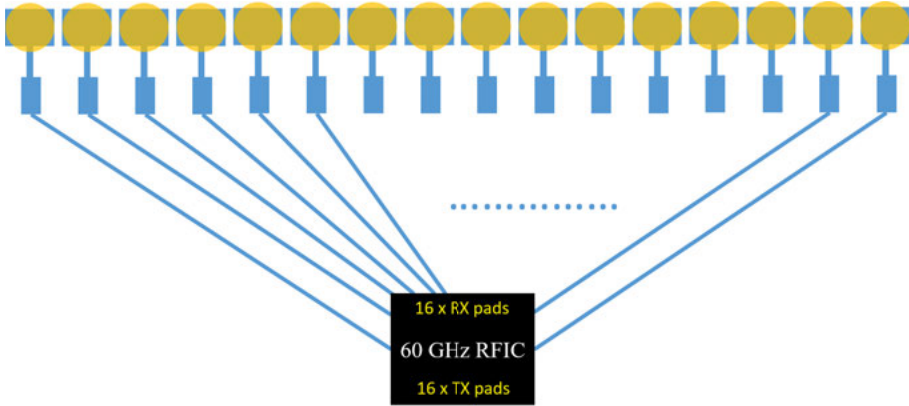

Fig. 4.2. 60 GHz RFIC integrated with 16 × element RX stacked patch antenna array. Same can be repeated on the TX side.

The idea of integrating the RFIC with the antenna array is presented in Fig. 4.2 where the RFIC is feeding 16 × columns of a single element stacked patch antenna at the RX side. The TX side will look similar. As the array has 16 × columns in the azimuth (H) plane, it will result in a narrow directive beam. However, having a single patch in the elevation (E) plane produces a wider beamwidth, so different options are investigated to reduce this beamwidth.
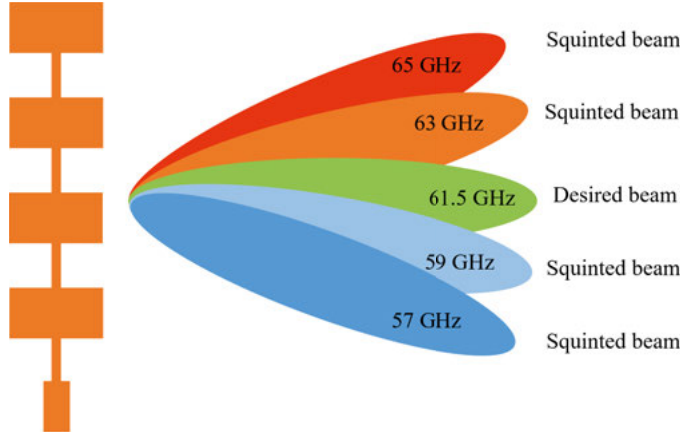
Fig. 4.3. Beam squint as a function of frequency for series fed antenna array.

A series array is more compact and does not create any space problems when $16 \times$ columns are placed side-by-side. However, radiation beam of a series array squints as a function of frequency. This is because the elements of the array are fed with different phases when moving from 57 to 66 GHz. As shown in Fig. 4.3, the array designed for 61.5 GHz center frequency radiates in the desired broadside direction. However for frequencies lower and higher than the center frequency, the phases at the input of each patch are either progressively increasing or decreasing, which makes the beam shift away from the broadside. The farther is the frequency of operation from 61.5 GHz, the higher is this beam squint. The beam squint could be useful for certain applications, e.g., radar communication, but is not desired for broadband communications.

It is further analysed that the beam squint gets worst for series arrays having more than two number of elements. So, instead of using a 4-element series array, a 4-element centrally fed series array is designed which keeps the beam squint to an acceptable level as well as decreases the elevation plane beamwidth. Fig. 4.4 (a) shows the single element stacked patches antennas which are used as building block for the other arrays. Both elements use rectangular patches as the feeding patch while parasitic patch is circular in one case and rectangular in the other case. The same structure of stacked patches is repeated to design 2-element series arrays, 4-element centrally fed series arrays and 4-element compact corporate array shown in Fig. 4.4 (b), (c), (d) and (e) respectively. The 2-element array on the left (circular patch over rectangular) is integrated with the 60 GHz RFIC [36] and the beam-steering results with the EIRP are presented in papers I and IV.
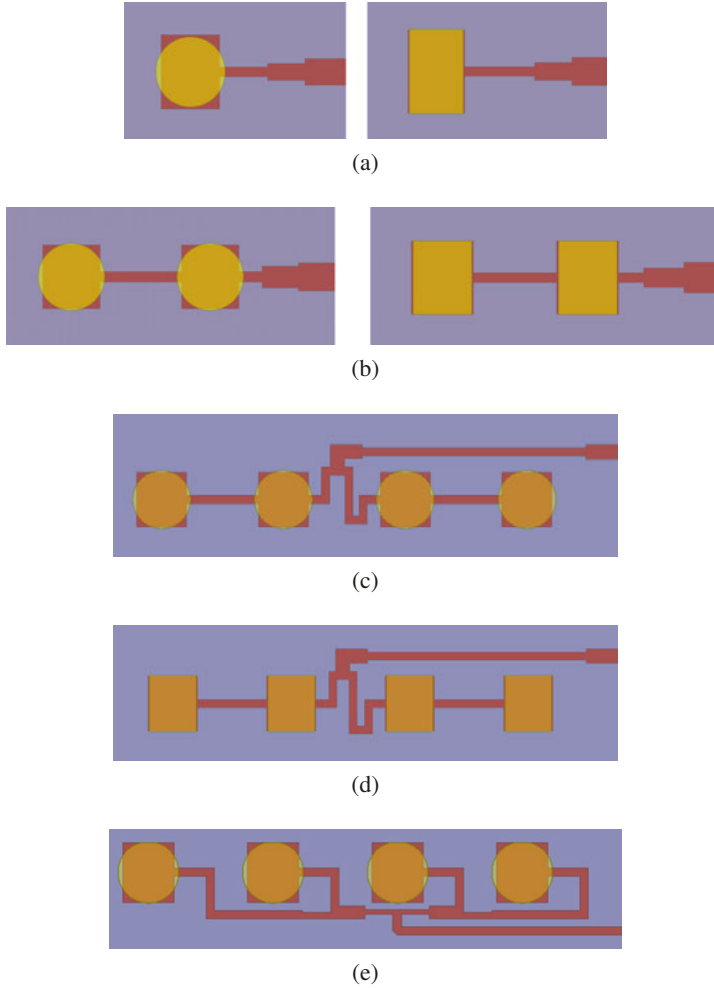
(a)

(b)

(c)

(d)

(e)

Fig. 4.4. Top view of the stacked patches antenna elements and arrays (a) Single element antennas (b) 2-element series fed antenna array (c) 4-element centrally fed series array with circular patches on top of rectangular patches (d) 4-element centrally fed series array with rectangular patches both on top and bottom (e) Compact 4-element corporate fed array with circular patches on top of rectangular ones.

4.3 Connected Slots Antenna Array (CSAA) Feeding High Gain Lens at 60 GHz

This section presents a high gain 60 GHz beam-steered antenna array designed mainly for mobile backhaul communications where all nodes are at the same height, so the elevation plane will have a fixed narrow-beam whereas the beam will be steered in the azimuth plane. The feed-switchable antenna arrays feeding the lens have been largely reported in the literature [44–48], however, the beam can only be steered to the predefined angles with this technique, and the link can break if the orientation of antenna changes from its predefined position. This is true especially if we talk about the narrow-beam backhaul communications. Instead this work proposes a linear phased antenna array to feed a dielectric lens antenna, where the feed will not only have significantly higher gain compared to the single element used in feed-switching, but will also allow to steer the beam to any arbitrary angle in $\pm 45°$ range with the help of front-end RFIC. Moreover, excitation of 16-paths at the same time results in spacial power combining and will increase the effective isotropic radiated power (EIRP) by 12 dB compared to single element excitation, as doubling the number of excitations results in a 3 dB rise.

The connected slots PCB array presented in Fig. 4.5 (a) will feed the lens shown in Fig. 4.5 (b) and (c). For characterization of the prototype, a 1:16 power splitter is designed to feed the connected slots array at sixteen equidistant points. This linear array extends along the y-axis, which will act as a point source in the elevation plane as can be seen in panel (b) of the figure. The lens thus plays major role in this plane to reduce the beamwidth. Besides, as connected slots array is extended along L_{Lens} in the azimuth plane [shown in panel (c) of Fig. 4.5], the beam will be steered in this plane with the help of RFIC. However, for performance verification, three different power splitters, shown in Fig. 4.6, are designed to steer the beam at 15°, 30° and 45° apart from the power splitter shown in Fig. 4.5 (a) which corresponds to broadside radiation (0°).

When all 16 feed points on the connected slots antenna array (CSAA) are excited in phase (0° beam), it is mainly the array itself which produces a 10° HPBW in the azimuth plane and the lens has no contribution in it. However, when the CSAA is excited to steer the beam away from the broadside in the azimuth plane, the hemispherical terminations of the lens play their role to enhance the gain. For usual phased arrays, the gain reduces with higher beam-steering angles because of angular dependence of element radiation pattern, called scan loss [49]. However, in our case, the gain increases up to certain beam-steering angles because of hemispherical terminations of the lens. Paper III contains further details in the Fabrication and Measurement section.
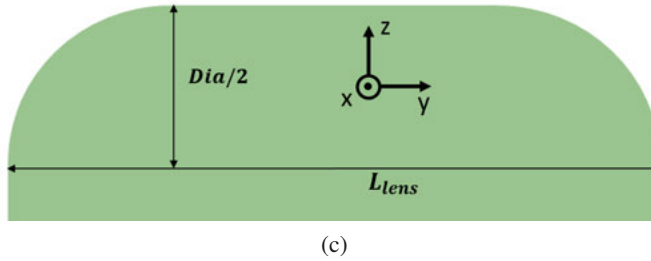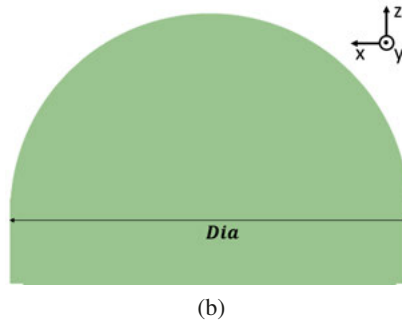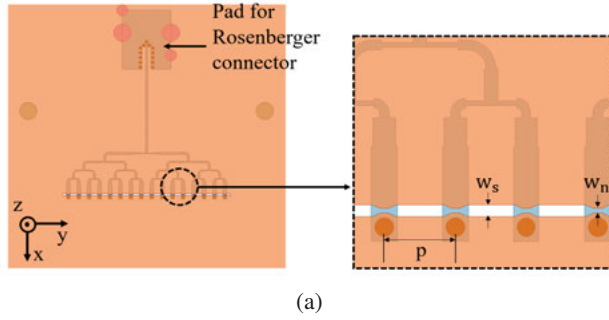
(a)

(b)

(c)

Fig. 4.5. Design view of dielectric lens (a) Elevation plane (XZ) view (b) Azimuth plane (YZ) view of the lens antenna, the CSAA extend along Y-axis.
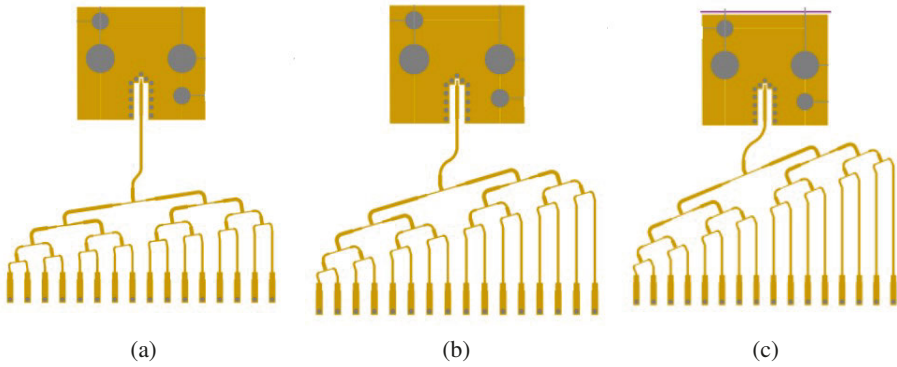

(a)   (b)   (c)

Fig. 4.6. Power splitters to steer the beam at (a) 15° (b) 30° (c) 45°.

4.4 Dipole Antenna Arrays: 28 GHz Antenna in Package (AiP)

The good performance PCB antenna arrays not only demand for low loss costly substrates, but also cause more integration losses with RFIC because of increased transmission line lengths and transitions from chip to the antenna. Moving from sub-6 GHz bands to millimeter wave bands makes the antennas more compact as physical dimensions are directly proportional to the operational wavelength. This allows to design antennas and antenna arrays directly in the RFIC package, which not only reduces the additional PCB cost but also reduces the interconnect lengths. This section discusses the design of two separate antenna arrays, a linear polarized dipole array and a circular polarized crossed dipole array, both working at 28 GHz for high data rate applications.

4.4.1 RFIC package

The smallest chip package that is of the same size as the chip is called fan-in wafer level package (FIWLP) shown in Fig. 4.7 (a). In the traditional assembling process, individual dies are packaged after dicing them from a wafer, while in FIWLP technology the integrated circuit (IC) is packaged at the wafer level by using the wafer fabrication processes and tools [50]. As this is a true chip scale package (CSP), the package allows only for limited number of interconnect solder bumps for DC and high frequency signals. In comparison, panel (b) of the figure presents an enhanced version of standard wafer level package, called fan-out wafer level package (FOWLP). The fan-out region in the FOWLP not only allows for more interconnect bumps for connectivity between chip and PCB but it also allows to place antennas / antenna arrays on re-distribution layer (RDL) in this region.

Different fan-out antenna designs have been presented in [51–63] at millimeter waves. Most of the designs presented in the above reference list are realized by using either multiple RDLs, double mold, through mold VIAs, or with an airgap in the mold. These variations increase complexity of the package, thus making it cost-ineffective.

The 28 GHz RFIC package used in this work is presented in Fig. 4.8. The 0.5 mm ball-grid array (BGA) package comprises of a single mold layer, three passivation (PSV) layers (PSV1, PSV2 and PSV3) and two RDLs (RDL1 and RDL2) [64]. The dummy solder bumps under the fan-out region are required for mechanical stability of the package. Presence of these dummy balls in the fan-out region has been investigated by simulating a microstrip patch antenna with and without the solder balls in the substrate. Adding these balls in the substrate results in slight increase in the dielectric constant which has been taken into account while designing the antenna array. This embedded wafer level BGA (eWLB) package has 12.6×12.6 mm^2 dimension while the die
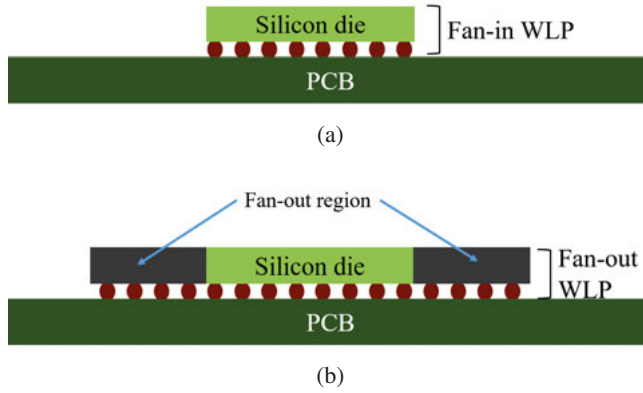
Fig. 4.7. Cross-sectional view of the wafer level packages (WLP) (a) fan-in WLP (b) fan-out WLP.

covers around 4.5×4.5 mm^2. This leaves with 12.6×4.05 mm^2 space on each side of the die to design the antenna arrays.
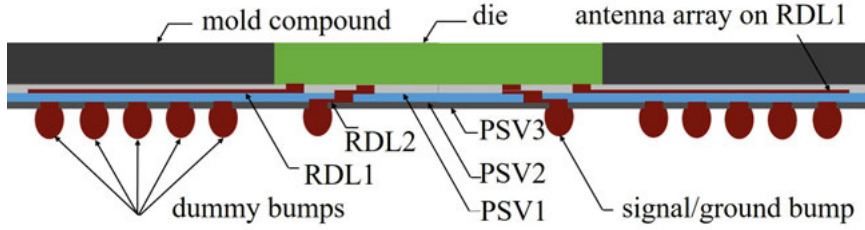

Fig. 4.8. Cross-section of the fan-out WLP used in the project, containing three passivation (PSV) and two re-distribution layers (RDL).

4.4.2 Linear polarized dipole array

Placement of different antenna elements in the fan-out region has been investigated, which suggests the use of a dipole antenna because of space constraints and wide beamwidth in the H-plane. As shown in Fig. 4.9, both TX and RX antenna arrays are identical and comprise of four dipole elements, placed at RDL1 in the embedded wafer level ball grid array (eWLB) package. The mutual coupling between the elements is significantly reduced with the help of a narrow metallic strip placed on RDL2 in the middle of every two dipole elements. Fig. 4.10 shows the mutual coupling between two neighboring dipole legs. It can be seen that the difference is around 5 dB in the shown frequency band and this reduction in mutual coupling significantly helps to improve the impedance bandwidth of the array.
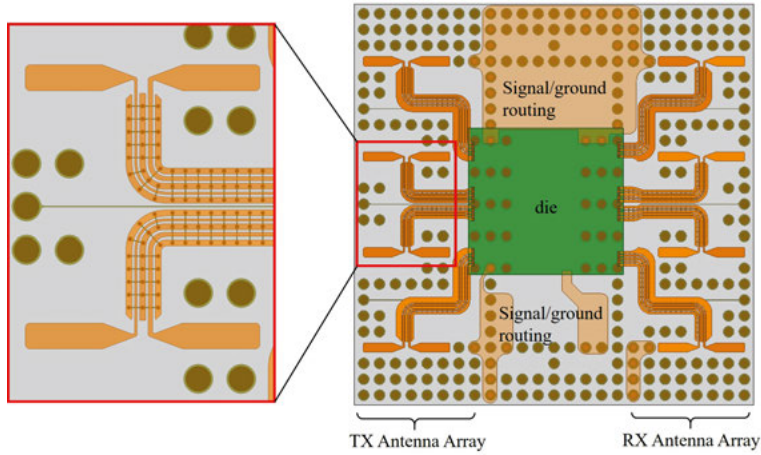
Fig. 4.9. TX and RX antenna arrays placed at RDL1 in the fan-out area of the 12.6×12.6 mm^2 package. The inset shows the zoom-in view.

The intended direction of radiation is through the mold, so to suppress the back lobe radiations, localized reflectors are placed at quarter wavelength distance from the antenna array in the FR-4 PCB, as shown in Fig. 4.11. Moreover, to suppress the surface wave propagation inside FR-4, a rectangular cavity is introduced with the help of PCB VIAs.
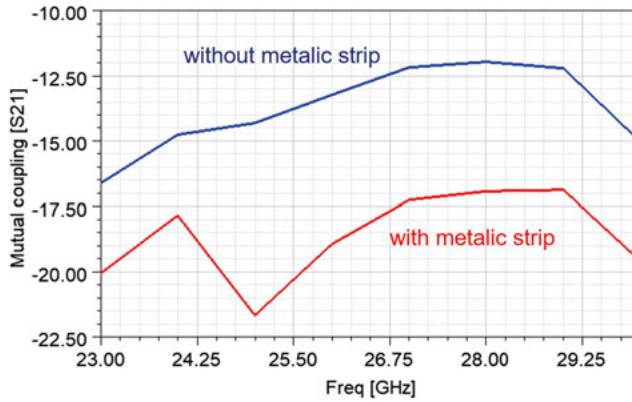

Fig. 4.10. Mutual coupling between dipole legs with and without the narrow metalic strip placed in the middle on RDL2.

Horn shaped heatsink

The presence of the heatsink cannot be neglected in the antenna array design as it is a key requirement in cooling down the active chip. As the heatsink

33

needs to be attached with the chip, it stays in close proximity to the antenna array which affects the radiation performance of the array. So, it is necessary to take into account the presence of the heatsink while designing the antenna array and this could turn in a positive asset. In this work, the heatsink is shaped as a horn antenna shown in Fig. 4.11, which not only dissipates the heat from the chip but also improve the radiation performance of the antenna arrays.
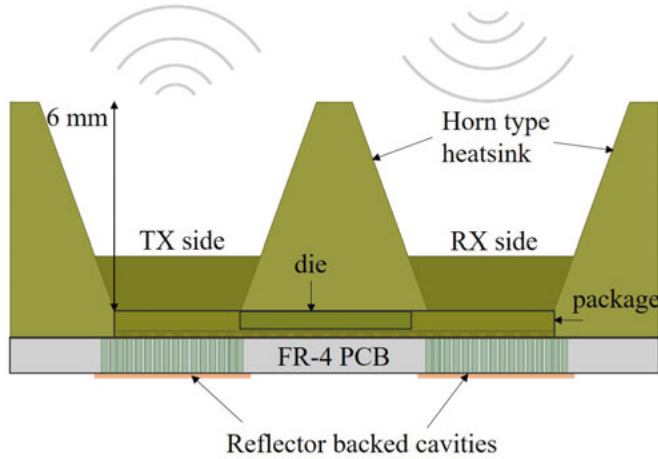

Fig. 4.11. An aluminium heatsink placed on top of the chip package. Reflector backed cavities are also shown in the FR-4 PCB.

4.4.3 Circular polarized crossed dipole array

Apart from the linear polarized array, a circular polarized antenna array is designed in the package for 28 GHz 5G applications. A crossed dipole is well known for its circular polarization and dual polarization characteristics [65–69]. Fig. 4.12 (a) presents the crossed dipole antenna arrays in the package and the zoom-in view shows the dipoles are fed through planar differential pairs coming from the chip pads. The lengths of the two dipoles in a crossed dipole are kept different from each other as suggested in [69] and this difference is further optimized to get the axial ratio less than 3 dB. Moreover, to get the directional coverage towards the broadside direction and suppress the back radiation, a reflector layer is introduced in the PCB at a quarter-wave distance from the dipole array as shown in Fig. 4.12 (b). A half-cylindrical aluminium heatsink is placed on top of the die for heat dissipation.
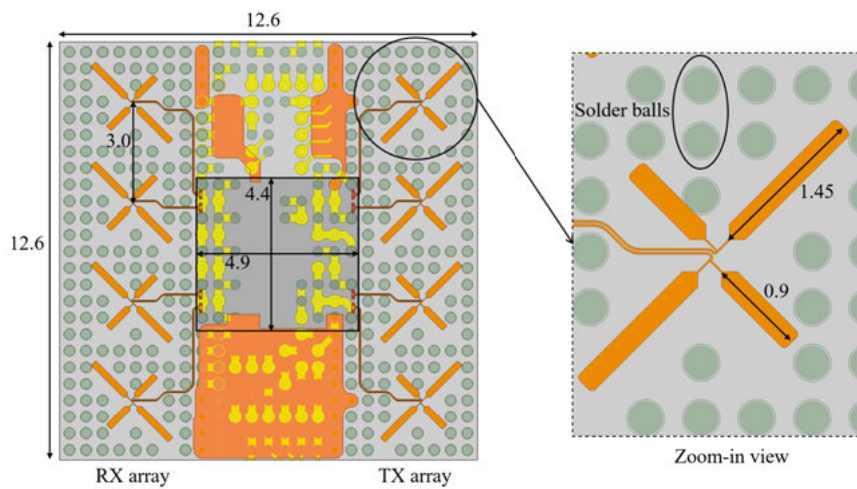
(a)
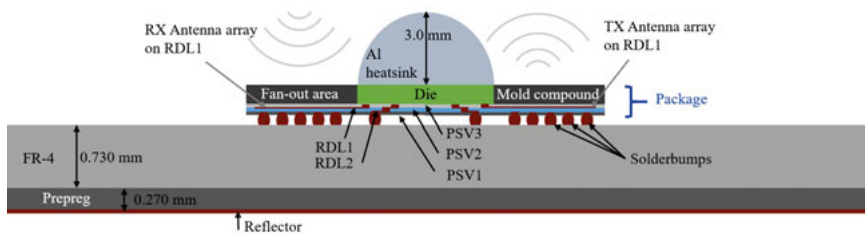
(b)

Fig. 4.12. Package layout. (a) RX and TX antenna arrays are designed on left and right to the chip, respectively. The inset shows the zoom-in view of the antenna element. All the dimensions are in mm. (b) cross-sectional view of the package integrated with the FR-4 PCB and a heatsink placed on top of the die.

5. Measurement Methods

5.1 Reflection Coefficient

The reflection coefficient defines how much power is reflected back due to impedance mismatching in the transmission path. Equation 5.1 defines the reflection coefficient (Γ) in terms of load and characteristic impedance.

$$\Gamma = \frac{Z_\mathrm{L} - Z_0}{Z_\mathrm{L} + Z_0} \tag{5.1}$$

where Z_L is load impedance and Z_0 is characteristic impedance. If load and characteristic impedance are matched (are the same), $\Gamma = 0$, i.e., no reflection occurs and maximum power is transferred from source to load. When Γ is expressed in terms of S-parameters, it is referred to as S_{11}.

In this thesis, the Vector Network Analyzer (VNA) Keysight PNA N5225A is used along with the millimeter wave OML extension modules [70] to measure the impedance matching of the antennas and antenna arrays. Fig. 5.1 shows the above mentioned network analyzer connected with the WR-15 (50 to 75 GHz) extenders. The measurements are carried out using coaxial port as well as ground signal ground (GSG) probe after performing the one-port short-open-load (SOL) calibration.
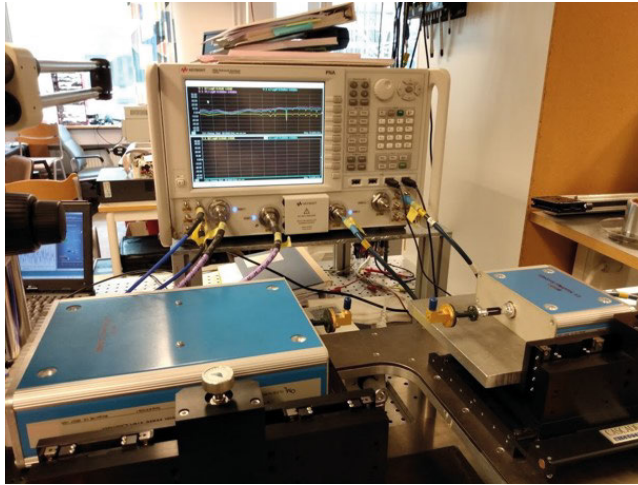

Fig. 5.1. Setup to measure the S-parameters.

5.2 Gain

Gain is an important characteristic in defining the performance of an antenna that describes the maximum radiation in a certain direction in relation to an isotropic antenna. The gain is usually presented in dBi where 'i' stands for isotropic. In this thesis, gain-transfer or gain-comparison method [24] is used to measure the gain of antenna arrays. These measurements are carried out with the help of the Keysight PNA N5225A along with millimeter wave OML frequency extenders. Waveguide S_{21} calibration is performed on OML extenders and the losses of the waveguide to coaxial transition and coaxial cable are measured separately. These losses are then taken into account during post-processing gain calculations. Three antennas are used in these measurements as shown in Fig. 5.2, where the transmitting antenna can be of any type or gain, while the receiver antenna is switched between standard gain horn and antenna under test (AUT). Input power at the transmitter side should be the same for both receivers and the system disturbances should be minimum when switching between the receiving antennas. The gain of AUT can then be calculated by using the FRIIS equation:

$$G_{AUT} = G_S + P_{AUT} - P_S \qquad (5.2)$$

where, G_{AUT} is the gain of AUT, G_S is the gain of standard horn antenna, P_{AUT} is power received by AUT and P_S is the power received by standard horn antenna. All values are in dB.

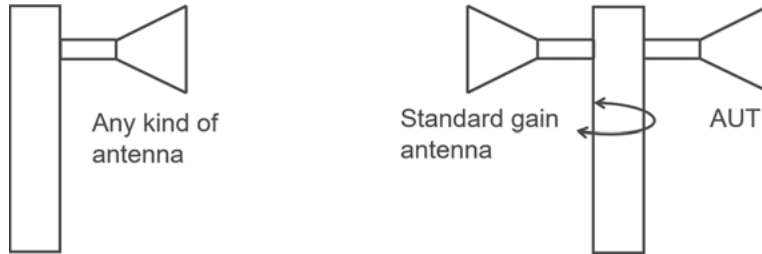Fig. 5.2. Setup to measure the gain using gain comparison method. TX is on the left while RX on the right.

5.3 Radiation Pattern

In 2D radiation patterns, azimuth and elevation plane measurements are the most common representations of an antenna. Two different methods are used in this work to measure the radiation pattern, 1) rotate the AUT around its center when the standard antenna remains stationary [Fig. 5.3 (a)] 2) rotate

the standard horn antenna around the stationary AUT [Fig. 5.3 (c)]. When measuring the far-field radiation patterns, the second method is feasible for millimeter and sub-millimeter wave measurements where the far-field distance to the antenna is not very high. The physical setup for the aforementioned methods is shown in Fig. 5.3 (b) and (d), respectively.
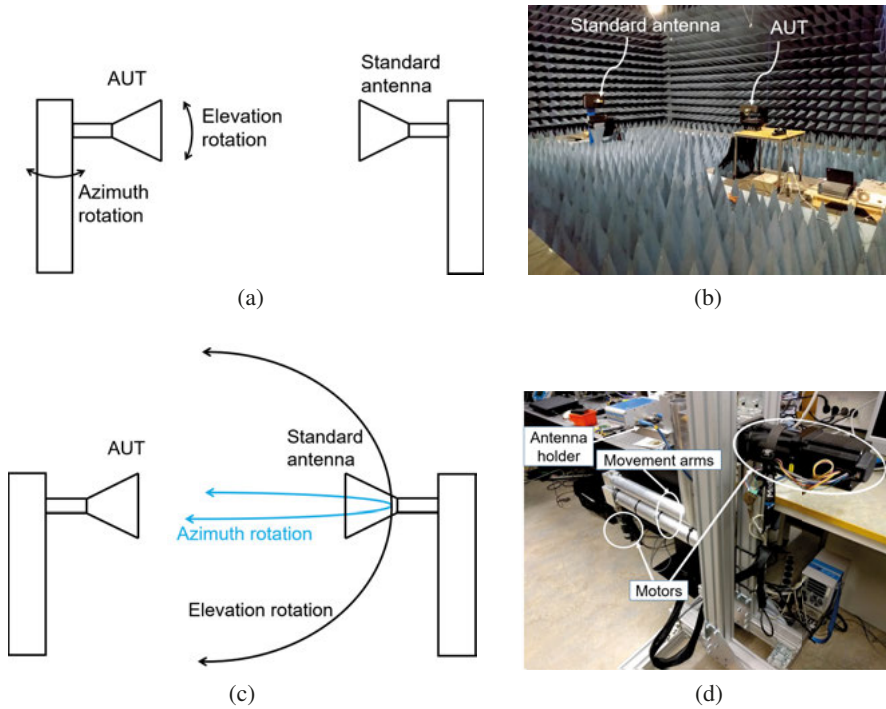

Fig. 5.3. Antenna radiation pattern measurement setup. (a) AUT is rotated in azimuth and elevation plane so the distance from the standard antenna remains constant. (b) Actual measurement setup for schematic shown in (a). (c) AUT is stationary and standard antenna is rotated in the azimuth and elevation plane around the AUT in large circles in such a way that the distance to the AUT remains constant. (d) Actual measurement setup for schematic shown in (c).

5.4 Polarization

The polarization of an electromagnetic (EM) wave is defined by the orientation of the E field component in the plane perpendicular to the direction of propagation. As shown in Fig. 5.4 where z is the direction of wave propagation, the wave is said to be linear polarized if the E-field varies linearly [(as in panel (a) of the figure]. The linear polarized wave could be horizontal, vertical or oriented any other angle. Likewise, looking in the plane perpendicular to

the direction of propagation, the wave is said to be circular or elliptical polarized if the E vector-head makes a circle [as in Fig. 5.4 (b)] or ellipse [as in Fig. 5.4 (c)] in that plane, respectively.
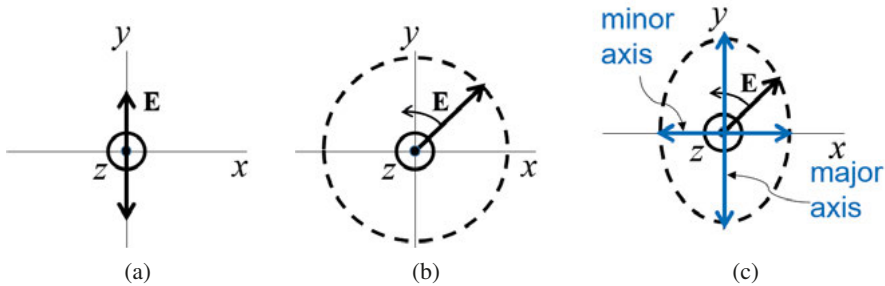

Fig. 5.4. Illustration of different polarizations. (a) Linear (b) Circular and (c) Elliptical polarization.

5.5 Polarization Measurement

For a linear polarized antenna, two radiation patterns are of great interest; co-polarization and cross-polarization patterns. As the name suggests, co-polarization radiation pattern of a linear polarized antenna is measured by placing AUT and standard antenna in a way that their E-field vector has the same orientation. Whereas to measure the cross-polarization radiation pattern, any one of the two antennas is rotated by 90°. The higher is the isolation between co- and cross-polarization measured power levels, the better linear polarized is the AUT.

5.5.1 Axial ratio measurement

Most practical circular polarized antennas are not purely circular but rather elliptical polarized, having a major and a minor axis as shown in Fig. 5.4 (c). The ratio of major to minor axis is called the axial ratio (AR) of the antenna. The value of AR can be between 0 dB (for pure circular polarized antenna) and ∞ (for pure linear polarized antenna).

The measurement setup for the AR of an antenna is shown in Fig. 5.5, where the linear polarized (LP) antenna is rotated around its center in the plane perpendicular to the direction of propagation, and power level is measured at different steps during this rotation. As an example, for an AUT that is broadside directed, Fig. 5.6 (a) shows the power levels measured at every 6 degrees in the above mentioned rotation, resulting in an ellipse. The axial ratio and the orientation of major axis can be determined by the normalized polar
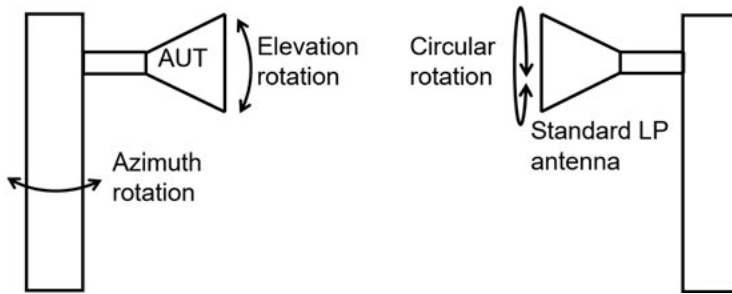
Fig. 5.5. Axial ratio measurement setup.

plot shown in Fig. 5.6 (b). Likewise, the AR of AUT can be determined for different angles of interest in the azimuth and elevation plane.

(a)

(b)
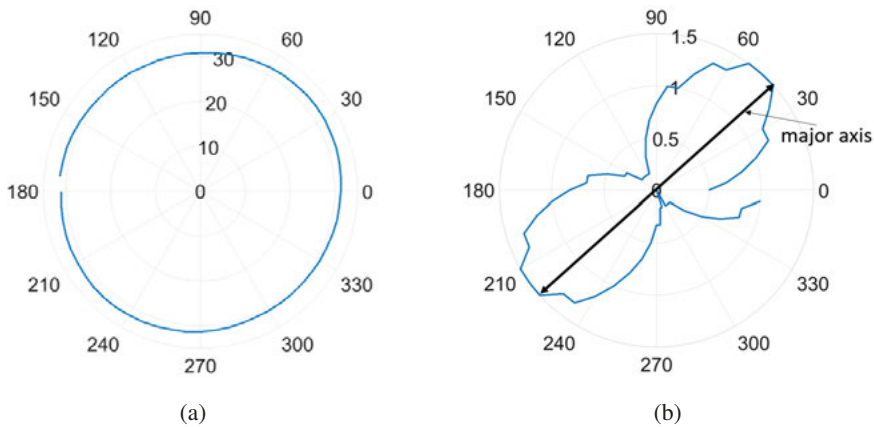
Fig. 5.6. Axial ratio plot of a circular polarized antenna array at 28 GHz. (a) Relative power levels shown in polar plot, (b) normalized power levels identifying the axial ratio and orientation of major axis.

5.5.2 Polarization radiation pattern

The measured radiation pattern containing the information of power levels as well as axial ratios for all angles in the plane of interest is known as polarization radiation pattern, as shown in Fig. 5.7. This can be measured with the help of the setup shown in Fig. 5.5, where AUT is set to a specific angle in the plane of interest and the standard LP horn antenna is rotated to measure the power levels for different orientations, as performed in the AR measurement. After completing a one complete round, AUT is set to next angle and LP antenna is again rotated in the complete circle to record the power levels for different orientations. This measurement is repeated in the same way for

different angles of AUT to obtain the radiation pattern shown in Fig. 5.7. Difference in top and bottom power levels at a specific angle shows the AR at that angle.
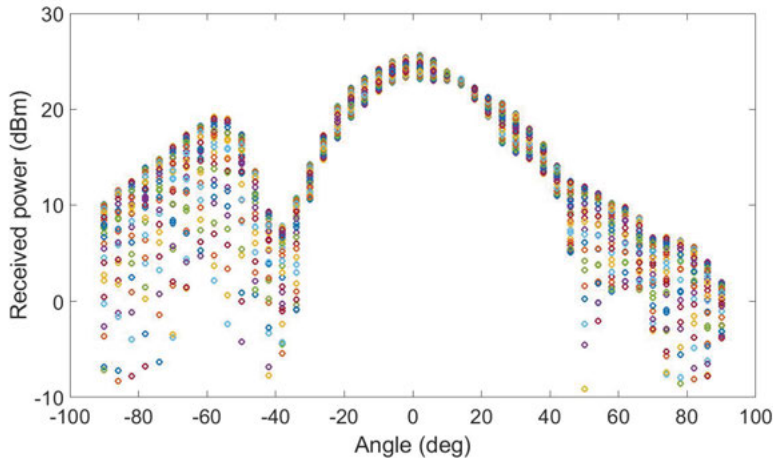
Fig. 5.7. Azimuth plane polarization radiation pattern of a circular polarized antenna.

5.5.3 Total power radiation pattern

When E vector rotates in a circle, every point on that circle has a vertical and a horizontal component, which means half of the power will be available in vertical orientation and the other half in horizontal orientation. Thus if a transmitter antenna is purely circular polarized, i.e., AR = 0 dB, a LP receiver antenna will receive half of the total available power (–3 dB). However, as most of the practical antennas are elliptical polarized, the total available power will be the sum of powers received in horizontal and vertical orientation by a LP antenna. It is also worth mentioning that this summation cannot be done in dB/dBm but the unit need to be converted to Watt/mWatt.

6. Beam-steering Measurements

This chapter presents the fabricated antenna array modules and prototypes. However the focus will be on the beam-steering measurement results for different antenna arrays presented in Chapter 4 of this thesis. But before presenting the beam-steering measurements, the generation of beamforming look-up table (LUT) is discussed in the first section.

6.1 Beam-book Generation

A beam-book or beamforming LUT contains the amplitude and phase information for each antenna element required to electronically steer the beam towards a specific direction (angle). As an example, if an 8-element antenna array is desired to have 15 different beams at some specific angles, the beam-book will have $8 \times 15 = 120$ total entries, where each beam will be defined with a set of eight specific amplitude/phase settings. The beam-book is usually stored in the chip and the entries are used to steer the beam towards the specific angles.
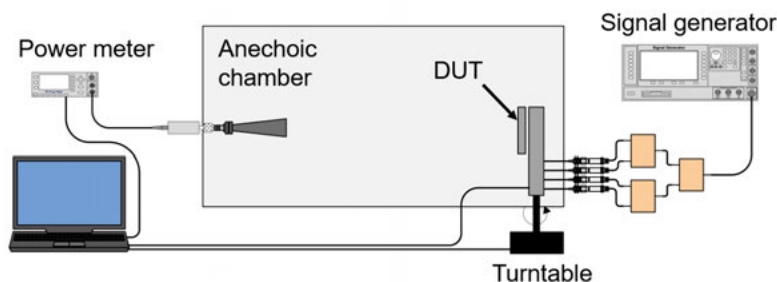
Fig. 6.1. Block diagram of measurement setup used to generate the TX beam-book.

Figure 6.1 shows the measurement setup used to generate the beam-book for the TX antenna array. For RX, the procedure is similar with the difference that the signal generator is feeding the standard horn antenna whereas a power meter measures the baseband signal power at the device under test (DUT) side. For an antenna array which requires 16 feeding paths from the chip, the algorithm can be broken down into the following steps:

1. Align the DUT/turntable to X degrees, where X is a specific beam angle in the beam-steering range [–50,...,50].
2. Set all the phase shifters to 0x1F1F which means no element is radiating power
3. Starting from the center, set the phase shifter of 8th antenna path (RF 8) to a fixed value, e.g, 0x0000
4. Sweep a set of constant amplitude phase shifter values for the RF 7 path. Measure the power received by the standard horn antenna for each value during the sweep.
5. Set the phase shifter of the RF 7 path to the value for which maximum power is received by the horn antenna and save this phase shifter settings
6. Repeat the steps 4–5 for RF 9, then RF 6, then RF 10 and in the same fashion towards the edge elements
7. Now that amplitude/phase has been optimized for all antenna elements, repeat the steps 4–6 while keeping the all elements activated. This will further improve the optimization process.
8. Move the DUT/turntable to next beam angle and repeat the step 1–7

6.2 60 GHz Stacked Patches Antenna Array

In this section, the beam-steering results for the stacked patch antenna arrays will be presented. The 2-element series fed antenna array shown in Fig. 6.2 (a) is used as building block for 2×16 antenna array shown in panel (b) of the figure. Two separate antenna arrays (2×16) are used for TX and RX as the RFIC has separate paths for TX and RX enabling full-duplex communication. Besides, panel (c) of the figure shows the evaluation kit[1] used to characterise the radio frequency module. A heatsink (black) is screwed on top of the chip for better heat dissipation.

The beam-steering measurement results for the array are presented in Fig. 6.3 for four WiGig channels centered at 58.32 GHz, 60.48 GHz, 62.64 GHz and 64.80 GHz. The phase shifters are set to maximum gain corner settings which makes the side lobe levels as high as –7 dB in some cases. The EIRP (effective isotropic radiated power) is more than +40 dBm for all channels in complete $\pm 50°$ range in azimuth plane. The 64 beams in $\pm 50°$ range should ideally be at $\approx 1.6°$ from the adjacent beam, while the measurement show that this value varies from $0°$ to $3°$. Moreover, the –3 dB beamwidths increase from $6°$ at the broadside to around $11°$ at extreme scan angles. This beam broadening comes from the array factor and is approximately inversely proportional to the cosine of the scan angle [71].

---

[1]https://www.sivers-semiconductors.com/wp-content/uploads/2020/11/Product-Brief-5G-mmWave-Test-Platform-new-profle-20201103.pdf accessed on 2020-12-14

(a) (b) (c)
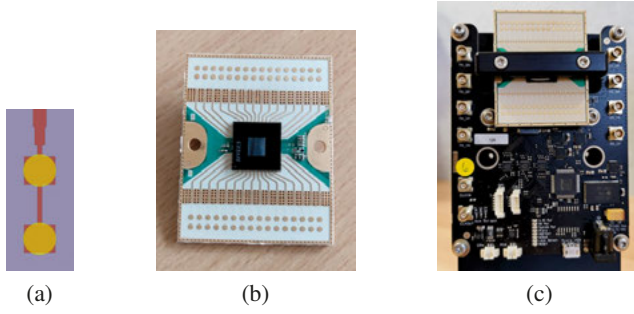
Fig. 6.2. 2×16 antenna array. (a) Top view of the 2-element series sub-array which is used as a building block of the 2×16 antenna array, (b) 2×16 PCB antenna arrays for TX and RX, integrated with the front-end RFIC in the center, (c) The RF module is attached on top of the evaluation board for characterization.

(a) (b)

(c) (d)
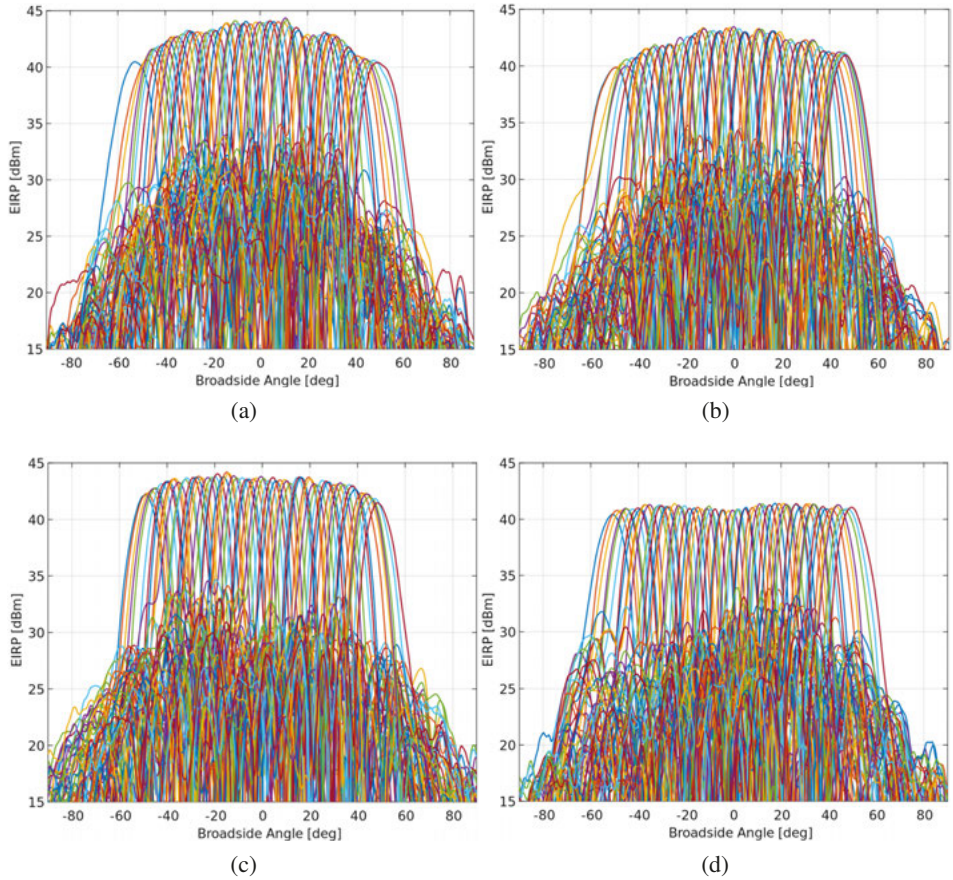
Fig. 6.3. A number of 64 beam radiation patterns of the four WiGig channels covered by the antenna module. The phase shifters are set to maximum gain and the signal chain is saturated (a) 58.32 GHz, (b) 60.48 GHz, (c) 62.64 GHz, (d) 64.80 GHz.

44

6.3 Connected Slots Antenna Array Feeding a High Gain Lens at 60 GHz

Fig. 6.4 (a) presents the fabricated dielectric lens while panel (b) shows the connected slots antenna array (CSAA) PCB screwed to the lens. The elevation plane measured radiation patterns for different frequencies are shown in Fig. 6.5, where the average half power beamwidth (HPBW) is 6°. The fabricated power splitter shown in Fig.6.4 (b) feeds every element on the CSAA with the same phase and amplitude, thus giving rise to the broadside radiation in the azimuth plane, shown in Fig. 6.6 (a). In the azimuth plane, the beamwidth is mainly dependent upon the 16-element CSAA thus resulting in 10° HPBW. Three more power splitters are designed (Fig. 4.6) and fabricated to characterise the antenna, Fig. 6.6 (b), (c) and (d) show the radiation patterns in the azimuth plane when beam is steered at 15°, 30° and 45°, respectively.

| (a) | (b) |
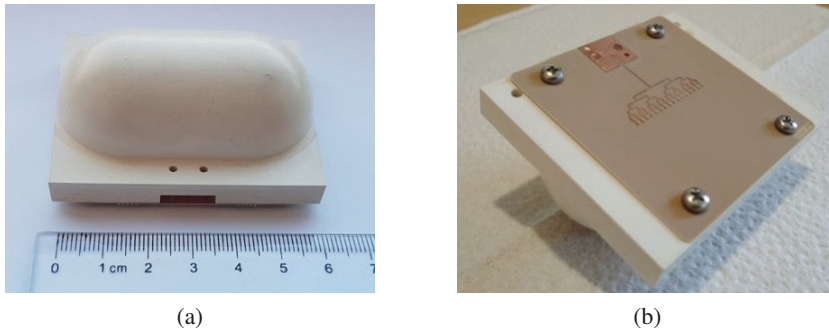
Fig. 6.4. Fabricated structures. (a) Dielectric lens, (b) connected slots antenna array PCB screwed to the lens.
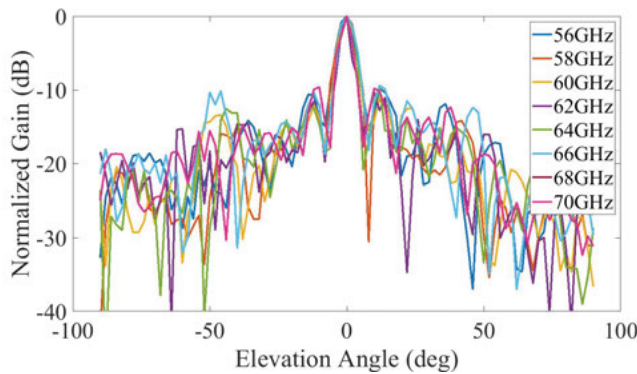
Fig. 6.5. Elevation plane (E-plan) measured radiation pattern for different frequencies between 56 GHz and 70 GHz.

Fig. 6.7, shows the peak measured gain as a function of frequency for different beams. For the 0° beam, the gain has 24.4 dBi maximum value with
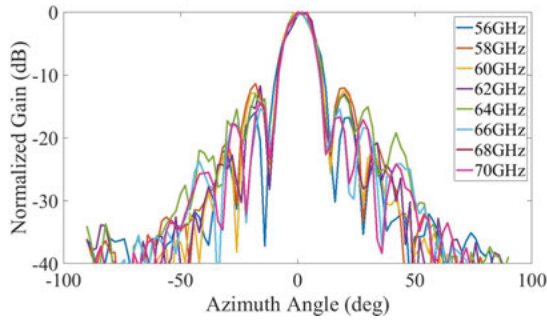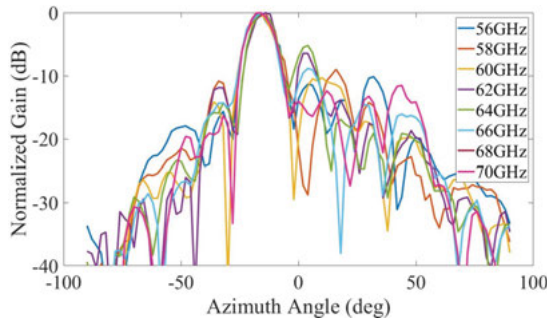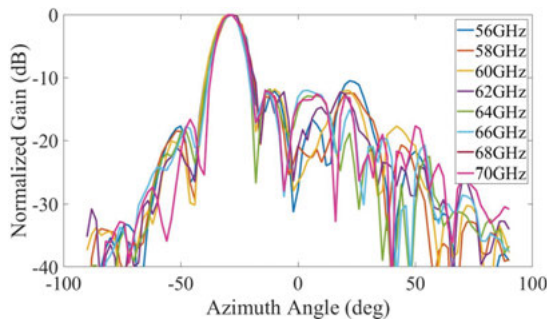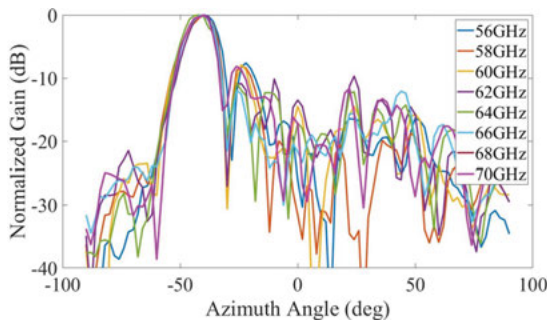
Fig. 6.6. Measured radiation patterns for different frequencies in the band when beam is steered at (a) 0° (b) 15° (c) 30° (d) 45°.

46

3 dB gain bandwidth over the full shown range. In traditional phased arrays, the gain reduces with the scan angle which is called scan loss [72], but in our case the hemi-spherical terminations of the lens help to increase the gain instead. This is the reason for that the gain for 15° beam is slightly higher than the broadside directed beam. This is more obvious when beam is steered at 30° the peak measured gain in this case is 25.4 dBi. The effect of the hemi-spherical terminations has started to diminish for 45°. The gain is lower compared to the other curves especially at higher end of the band.

The 3 dB gain bandwidth covers the entire 60 GHz band (57–66 GHz) for all beam-steering angles. Besides, the 3 dB beam-steering range is at least ±45° as higher angles are not measured.
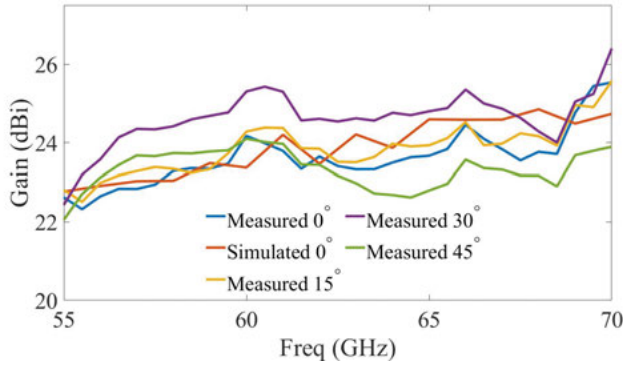
Fig. 6.7. Measured gain for all different beam angles along with simulated gain for the 0° beam.

6.4 Dipole Antenna Array

As discussed in Section 4.4, two dipole antenna arrays are designed at 28 GHz, one with linear polarization and the other with circular polarization. More details about these two arrays are given below.

6.4.1 Linear polarized dipole array

Fig. 6.8 (a) shows the fabricated antenna arrays in the package at re-distribution layer 1 (RDL1) where the dots on the package are the solder balls. The wave propagation direction is into the page for this panel of the figure. Panel (b) of the figure shows the radio frequency module where the the package is integrated with the PCB while horn-shaped heatsink is screwed on top of the PCB. The rectangular openings in the heatsink show the other side of the package which is black mold and transmission/reception is done through these open-

ings. Panel (c) of the figure shows the radio frequency module mounted on the evaluation kit for characterization.

<center>(a)   (b)   (c)</center>
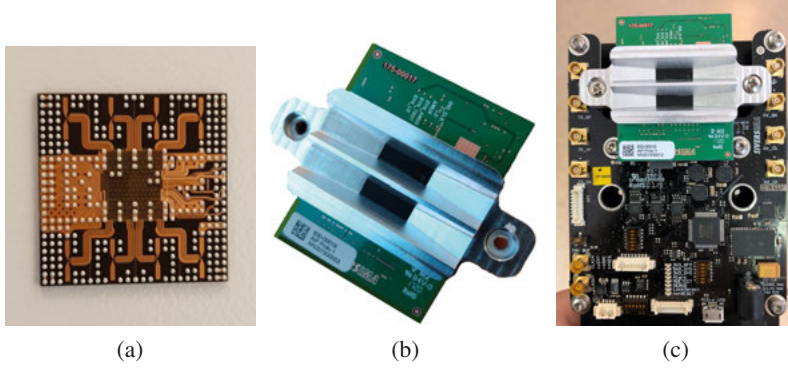
Fig. 6.8. The 28 GHz antenna in package (a) Full bottom view of the package (12.6×12.6 mm^2) is shown where antenna arrays can be seen on RDL1, (b) radio frequency module: the package is integrated with the FR-4 PCB with aluminium heatsink placed on top, (c) evaluation kit: radio frequency module is attached on evaluation kit for characterization.

Fig. 6.9 (a) and (b) show the elevation plane co- and cross-polarization radiation patterns at different frequencies in the 28 GHz band for RX and TX arrays respectively. The radio frequency module delivers 34 dBm maximum EIRP. The co- and cross-polarization isolation of the antenna array is around 25 dB in the broadside direction for the complete frequency band. Moreover, panel (c) and (d) of the figure show the 28 GHz measured beam-steering radiation patterns in the azimuth plane in $\pm 35°$ range. Seven different beams are measured in this range for both RX and TX, shown respectively.

6.4.2 Circular polarized crossed dipole array

Figure 6.10 (a) shows the fabricated circular polarized crossed dipole antenna arrays in the fan-out. The propagation direction is into the page for this panel. Panel (b) of the figure shows that the package is integrated with the PCB and the aluminium heatsink is also screwed on top of the PCB. The characterization of this module is also carried out with the same evaluation kit as shown in Fig. 6.8 (c) by placing the module on top of the kit.

Fig. 6.11 presents the polarization radiation pattern for the broadside beam in the azimuth plane. The pattern at 28 GHz is measured in the azimuth plane at 4° steps with 29 measurements at every step. The power difference between top and bottom values for any azimuth angle defines the axial ratio (AR) at that angle. Moreover, Fig. 6.12 (a) and (b) show RX and TX elevation plane radiation patterns for different frequencies in the band. The radiation is moved away from broadside for both cases but in opposite directions as both arrays

(a)

(b)

(c)

(d)

Fig. 6.9. Measured elevation plane co- and cross-polarized radiation patterns for different frequencies in the band (a) RX (b) TX. Azimuth plane beam-steering radiation patterns in $\pm 35°$ for (c) RX (d) TX.

(a)

(b)
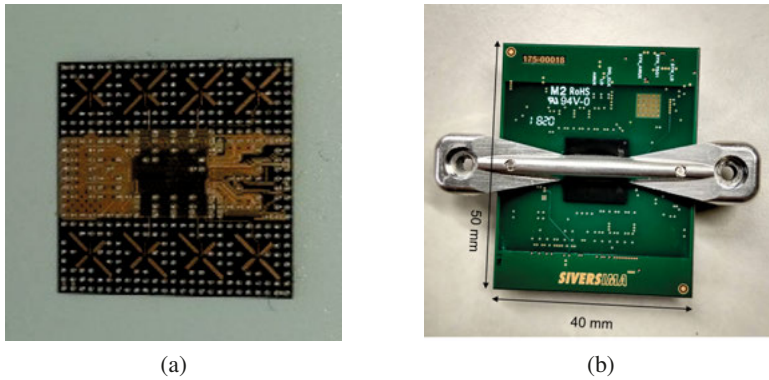
Fig. 6.10. The 28 GHz circular polarized antenna array in the package. (a) Full bottom view of the package (12.6×12.6 mm^2) is shown where antenna arrays can be seen on RDL1 in the fan-out region, (b) radio frequency module: the package is integrated with the FR-4 PCB and an aluminium heatsink placed on top.
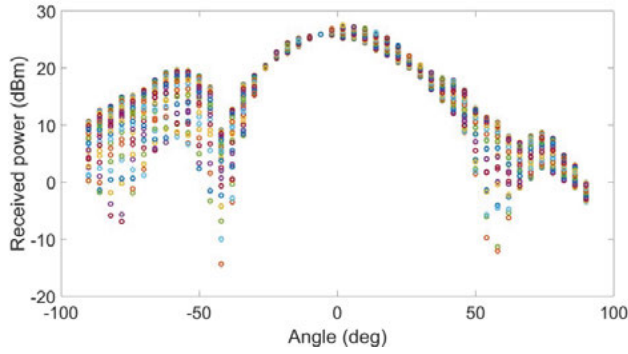
Fig. 6.11. Measured polarization radiation patterns for broadside azimuth beam for the TX at 28 GHz.

are placed on opposite sides of the chip and heatsink, which move the radiation peak away from the centre. This circular polarized module shows 31 dBm peak EIRP. The beam-steered radiation patterns measured at 28 GHz for RX and TX are shown in Fig. 6.12 (c) and (d) respectively. The beam-steering range is $\pm\,50°$ in the azimuth plane.

(a) (b)

(c) (d)
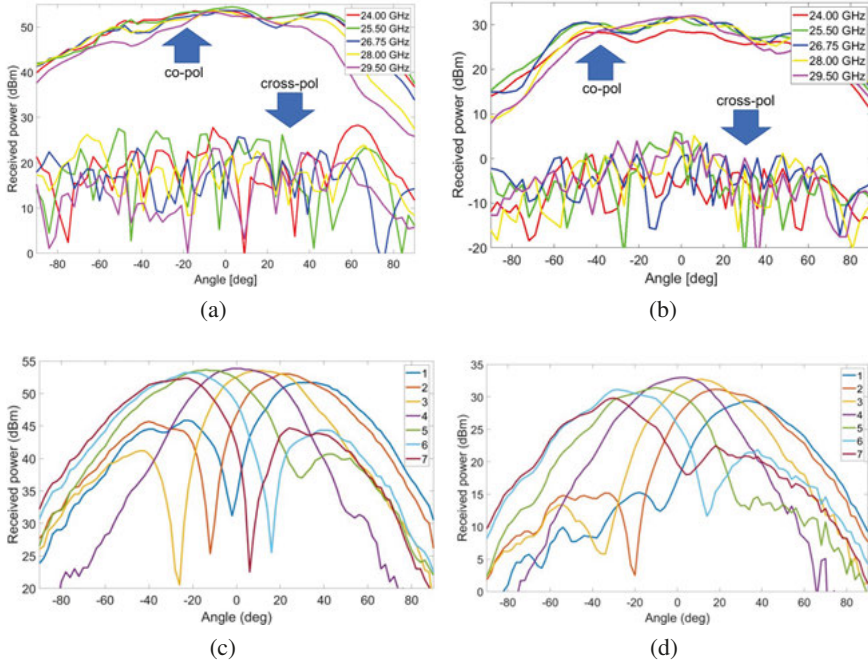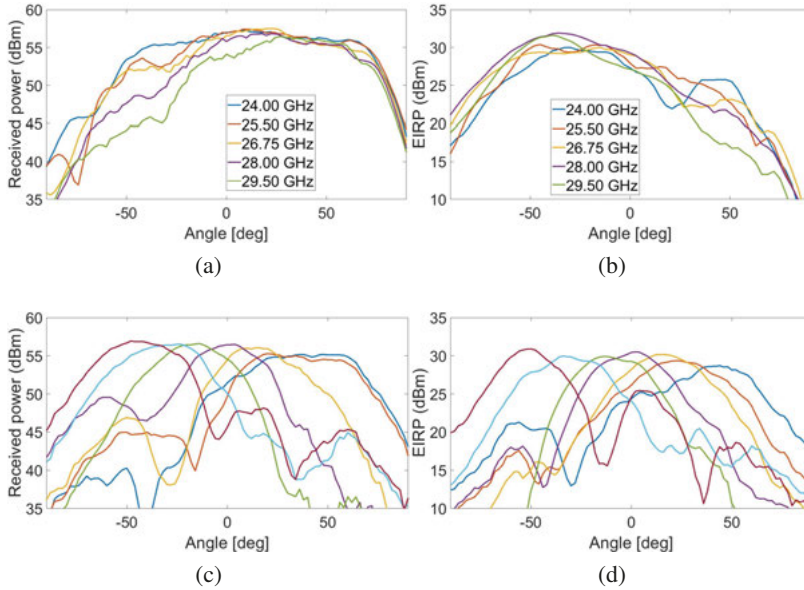
Fig. 6.12. Measured elevation plane radiation patterns for different frequencies at 28 GHz band (a) RX (b) TX. Azimuth plane beam-steering radiation patterns measured at 28 GHz in $\pm 50°$ for (c) RX (d) TX.

7. Measurements in Radiation Hard Environment

The use of wireless technologies in high energy physics applications require the technology to be radiation tolerant. In this chapter, the radiation hardness of a 60 GHz front-end transceiver chip is investigated using 17 MeV proton irradiation and 200 MeV electron irradiation. The chip is produced using 65 nm CMOS technology. Before going into specific details, the irradiation damages to silicon are discussed briefly in the first section.

7.1 Irradiation Damages in Silicon

Irradiation causes two type of damages in silicon, surface damages and bulk damages. Surface damages are caused by ionization at oxide/semiconductor (SiO_2-Si) interfaces while bulk damages are produced due to displacement of silicon atoms out of their lattice sites, which is illustrated in Fig. 7.1. A silicon atom can be knocked out of its lattice site by a particle having recoil energy $E_R > 20$ eV threshold [73], resulting in an interstitial (I) -vacancy (V) pair, also called Frenkel pair. This displaced silicon atom is known as *primary knock − on atom* (PKA) which can displace further atoms if it has enough energy. A PKA can cause the formation of about 1000 Frenkel pairs if it has an energy $E_R = 50$ keV [74]. A recombination of IV pairs can take place for 60% of total produced pairs while reaching 75%-90% in some disordered regions [75]. The uncombined pairs travel through the lattice and cause further reactions, thus causing real damage to the silicon bulk material which changes the electrical properties of the device.

Fig. 7.1. An illustration of displacement damage in silicon due to a high energy particle, where red arrows show the movement of the high energy projectile particle.

7.1.1 Total ionization dose and ionization damages

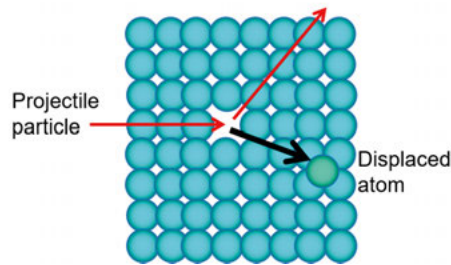Surface damages are caused by the ionization in silicon which happens due to the interaction of high energy charged particles with the atoms in the material [76]. Charged particles, like protons or electrons, generate electron-hole pairs in silicon that leads to ionization damages, where the density of electron-hole pairs is proportional to the energy transferred [77]. The energy transferred from charged particles to silicon is a function of particle mass, particle energy and silicon density [78] and has the units $MeV.cm^2/g$. This energy transfer is also referred to as stopping power. The stopping power/energy transfer is higher for protons than electrons up to 100 MeV but drops for higher energy values [78]. The total energy deposited by a particle causing the production of electron-hole pair is known as total ionization dose (TID). The SI unit for TID is Gray (Gy) where 1 Gy = 1 J/kg. TID is also expressed in terms of rad (radiation absorbed dose) where 1 rad = 0.01 Gy.

In CMOS devices, displacement of a single atom from silicon dioxide (SiO_2) does not cause a cascade reaction because of the irregular crystal structure of the oxide, however the ionization in the oxide can change the interface properties. When an electron-hole pair is generated in the oxide, electrons can move faster to the positive electrode because of their higher mobility compared to holes. The holes move slowly in the oxide due to large presence of shallow hole traps. This movement from one shallow trap to the next in the direction of electric field might result in a permanent hole trap if the hole reaches near Si-SiO$_2$ interface where many deep hole traps exist [79]. An illustration of the main processes involved in TID is shown in Fig. 7.2. Some of the trapped holes near the interface can recombine with electrons from silicon, which reduces the positive charge trapped in the oxide. This electron tunneling from silicon to oxide increases exponentially with decrease of oxide thickness, which makes thin oxide of deep sub-micron MOS transistors intrinsically more radiation tolerant than thicker oxides [80].
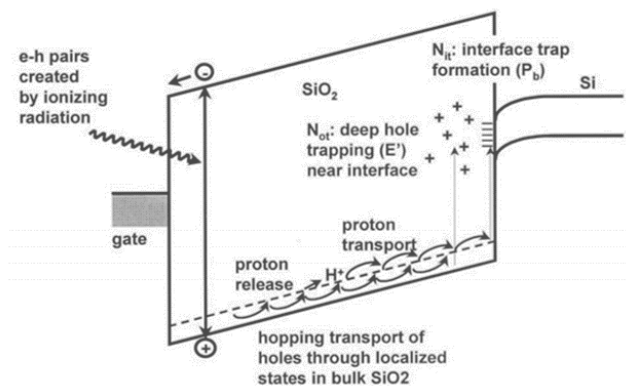

Fig. 7.2. An illustration of main processes in TID [79].

For CMOS devices, TID is usually reported as the most important concern [81] and the cumulative long term TID effect can cause threshold voltage shift, leakage current and deteriorated functionality [82].

7.2 Transceiver Chip Under Investigation

This section discusses the radiation hardness measurements of the 60 GHz transceiver chip (STuW60A2) designed in a 65nm CMOS technology. Fig. 7.3 (a) shows the block diagram of this short range chip which uses on-off keying (OOK) modulation scheme. The half-duplex chip requires 40 mW and 25 mW power in transmit (TX) and receive (RX) modes, respectively. The on-chip voltage controlled oscillator (VCO) generates a sine-wave signal around 60.5 GHz in the TX subsystem, while envelope detection is employed in the RX. Different test points can be seen in the figure used for analyzing the operation of the TX and RX before and after irradiation of the chip. The 25-balls fine-pitch ball grid array (BGA) package measures $2.2 \times 2.2 \times 1.0$ mm^3.

As shown in Fig.7.3 (b), a specific evaluation board is designed and fabricated where the necessary characterization is performed. The board is provided with $2 \times$ RF ports to be connected to the antenna along with digital TX and RX differential ports. The DLN-4M adapter provides USB port for PC/laptop.

7.3 Proton Irradiation at Turku

The proton irradiation was performed at Åbo Akademi University, Turku, Finland where the MGC-20 cyclotron was set to generate 17 MeV protons. Two evaluation boards were operational during the experiment, communicating at 5 Gbps generated with the help of Stratix V FPGA board. Table 7.1 shows the fluence and TID (total ionization dose) used for the RX and the TX.

Table 7.1. Measured fluence and dose used in the proton irradiation experiment.

DUT	Measured fluence	Measured TID
RX	1.38×10^{14} N$_{eq}$/cm^2	7.4 Mrad (74 kGy)
TX	0.78×10^{14} N$_{eq}$/cm^2	4.2 Mrad (42 kGy)

Fig. 7.4 shows the normalized power spectrum of 5 Gbps data transmission while transmitter is set to continuous wave mode. The pre- and post-irradiation characterization shows a small 10 MHz downshift in the centre frequency, however it does not affect the communication as the RX uses envelope detection.
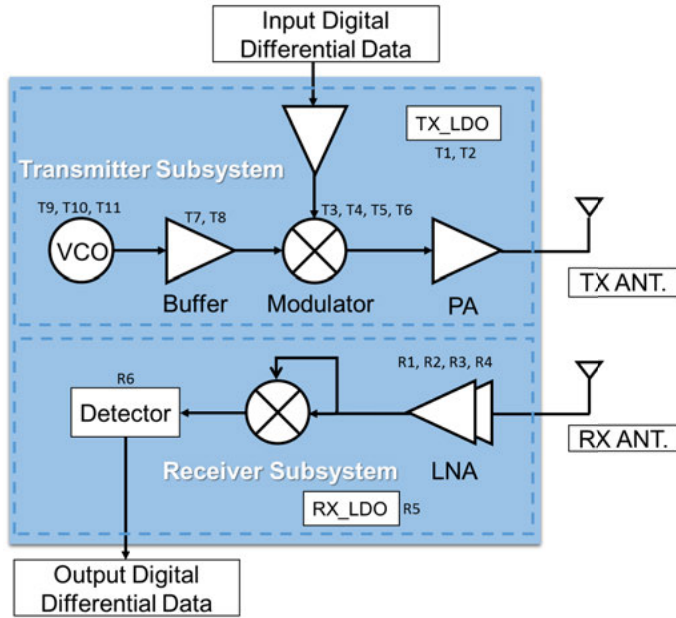
(a)
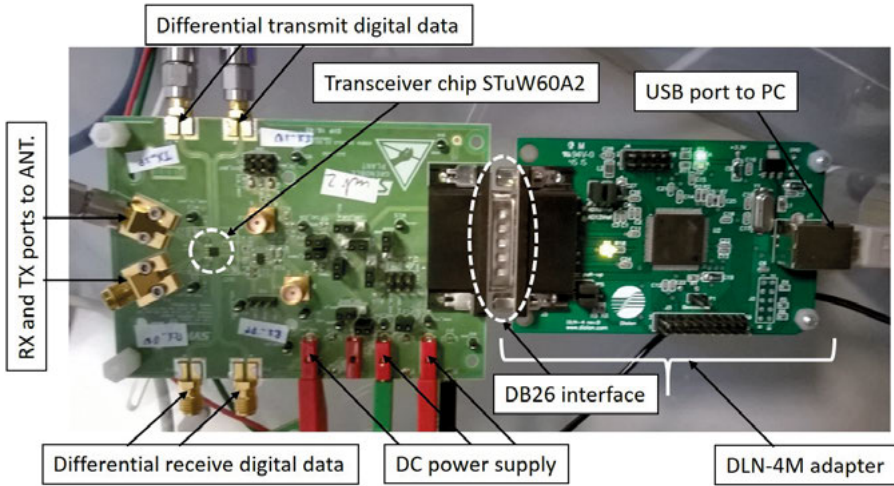
(b)

Fig. 7.3. 60 GHz transceiver chip and the evaluation board. (a) Block diagram of the chip, where T1 – T11 and R1 – R6 show analogue voltage test points for transmitter and receiver subsystems, respectively, (b) chip mounted on evaluation board, while DLN-4M adapter board providing DB26 to USB interface.
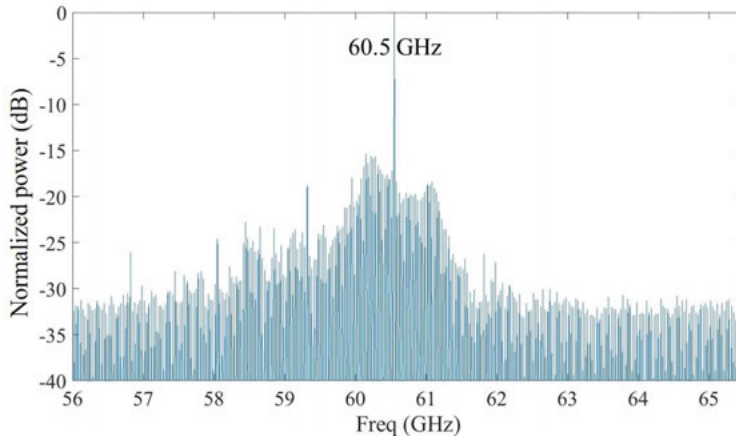
Fig. 7.4. Normalized power spectrum of 5 Gbps data transmission while transmitter is set on continuous wave mode.

A total reduction of 5.5 dB in the link budget was observed, out of which 4.5 dB belongs to RX as it was exposed to higher dose. Besides, the envelope detection in the RX as well as digital interface remained un-affected. More-over, 5 Gbps wireless communication was achieved in the post-irradiation analysis with a few cm reduced range.

7.4 Electron Irradiation at CLEAR, CERN

The electron irradiation is performed to study the radiation damage effect on the SiO_2-Si interface which is known to be the main failure mode for CMOS technology [81]. The electron irradiation allows studies at much higher doses than with protons because the irradiation area is much easier to constrain with the electrons compared to protons. The protons produce a large background of neutrons and activation that may damage the surrounding non-radiation hard electronics and measurement equipment used in the study.

Table 7.2. Calculated fluence and dose used in the proton irradiation experiment.

DUT	Measured TID
RX	270 Mrad (2.70 MGy)
TX	314 Mrad (3.14 MGy)

A 200 MeV electron irradiation is performed on the chip which is presented in Section 7.2 at CLEAR (CERN Linear Electron Accelerator for Research)

facility. Table 7.2 shows the TID used for RX and TX in the experiment. The pre- and post-irradiation characterization of the chips reveal an 80 MHz upshift in the centre frequency. An overall link budget degradation of 10 dB was observed which is a sum of 4 dB reduced TX output power and 6 dB degraded receiver sensitivity. Besides, circuit bandgaps (voltage reference) were degraded which also impacted the digital interface by changing the duty cycle. Despite the mentioned degradation, the chips were found operational in the post-irradiation characterization.

8. Summary

Rapid increase in wireless data demands ask for a shift towards millimeter-wave frequency bands. The availability of wider bandwidths at 28 GHz and 60 GHz allow to achieve these data demands but at the cost of increased propagation losses. High gain antenna arrays are required to compensate these losses, however, this results in reduced beamwidth, which calls for solutions with beam-steering realization.

In this thesis, we have presented different antenna arrays at 60 GHz and 28 GHz. These arrays are integrated with the front-end RFIC to steer the beam in $\approx \pm 50°$ in the azimuth plane. The 5G antenna arrays at 28 GHz are designed to provide the broadband high data rate services to the end users. These services will be available in places with high user density, as well as for homes and businesses with a fixed wireless access (FWA) network. To transport this high volume data to the core network, an FWA link requires the implementation of a broadband, high gain and steerable narrow-beam array. The 60 GHz antenna arrays, presented in this thesis, satisfy these conditions and can be used for both FWA as well as backhaul communications.

The proposed 60 GHz antenna arrays fall in two different categories: stacked patch antenna arrays (**Paper I, IV**), and connected slots antenna array feeding the high gain lens antenna (**Paper III**). The 2×16 stacked patch antenna array gives a realized gain of more than 20 dBi for all four WiGig channels. This PCB antenna array is integrated with the front-end RFIC which can feed each 2-element sub-array with specific weights (amplitude/phase) to steer the beam at any azimuth angle in $\pm 50°$ range. More than 40 dBm EIRP has been achieved for all four channels as well as in complete beam-steering range.

The other 60 GHz antenna array is designed by feeding a linear connected slot at sixteen equidistant points, which is then used as a feed to a high gain dielectric lens. The $16 \times$ feeds can steer the main beam in the azimuth plane when appropriate weights are provided. The beam-steering capabilities of the design are tested with the help of four different power splitters which are used to steer the beam at $0°$, $15°$, $30°$ and $45°$. Maximum measured gain of 25.4 dBi is achieved with this antenna. Moreover, instead of scan loss, the lens design provides higher gain when the beam is steered away from the broadside direction.

Furthermore, two compact antenna arrays are designed at 28 GHz (**Paper V, VI**) with relatively lower EIRP, thus focusing lower-range applications. A linear polarized and a circular polarized array are realized in the fan-out region using fan-out wafer level packaging (FOWLP) technology, thus forming

an antenna-in-package (AiP) solution. In comparison with the PCB antenna array, the FOWLP is not only cost effective but it also reduces the integration losses (from the front-end RFIC to the antenna array) because of shorter feed lines and no geometrical discontinuity. The linear polarized antenna array is realized as a dipole antenna array feeding a horn-shaped heatsink. The RF module gives 34 dBm maximum EIRP with beam-steering in $\pm 35°$ in the azimuth plane. The co- and cross-polarization isolation is around 25 dB for complete frequency band. Moreover, the circular polarized antenna array is realized with the help of crossed dipoles which gives less than 3 dB axial ratio in the 28 GHz band. The RF module provides 31 dBm maximum EIRP with beam-steering in $\pm 50°$.

The wireless data demands are not limited to the telecom industry as the upgradation of accelerators and experiments at the large hadron collider (LHC) at CERN will result in increased event rates thus demanding higher data rate readout systems. In this work, we have also investigated the feasibility of 60 GHz wireless links for the data readout at CERN (**Paper II**). Considering the radiation levels that a wireless front-end will encounter in such a harsh environment, the 60 GHz wireless chips are irradiated with 17 MeV protons [dose 7.4 Mrad (RX) & 4.2 Mrad (TX)] and 200 MeV electrons [dose 270 Mrad (RX) & 314 Mrad (TX)] in different episodes. The chips have been found operational in the post-irradiation investigations with minimal performance degradation in case of proton irradiation. However, the performance reduction is higher in case of electron irradiation due to high total ionization dose (TID). These encouraging results motivate to move a step forward and investigate the realization of wireless links in such a complex environment.

Sammanfattning på Svenska

Den snabba ökningen av behovet dataöverförings kapacitet i trådlösa nätvärk kräver en förskjutning av frekvensområdet mot millimeter-vågfrekvensbandet. Bandbredden för dataöverföring vid 28 GHz och 60 GHz är väsentligt större än det som erbjuds idag men en ökad kapacitet kommer på bekostnad av ökade utbredningsförluster för radiovågorna. För att nå hög förstärkning krävs sammankopplade antenner i matriser för att kompensera för dessa förluster. Detta ger högt fokuserade strålmönster vilket p.g.a. av den minskad strålbredden därför kräver att radiovågorna styrs med hög precision från sändare till mottagare.

I denna avhandling presenterar jag olika antennuppsättningar som opererar vid 60 GHz och 28 GHz frekvensbanden och teknik för att styra huvudstrålens riktning omkring ±50° i azimutplanet. Jag utvecklat två olika antenntyper för 60 GHz bandet nämligen: staplade sk. patchantennmatriser (**Publikation I, IV**) och anslutna kortantenner där antennen matas med hög förstärkning (**Publikation III**). De båda matriserna är väl lämpade för 60 GHz kommunikation mellan basstation och mottagare samt för åtkomstkommunikation. Den 2x16 staplade patch-antennuppsättningen ger en realiserad vinst på mer än 20 dBi för alla fyra WiGig-kanaler med strålstyrning som sträcker sig i ±50° i azimutplanet. För en kretskortsintegrerad antennuppsättningen där en radiofrekvent integrerad krets (RFIC) vid 60 GHz matar varje par av element i en undergrupp av flera element med specifika vikter (amplitud / fas) kan strålen styras i valfri vinkel inom ett 100° intervall. Mer än 40 dBm effektiv isotropisk strålningseffekt (EIRP) har uppnåtts för alla fyra kanalerna och över hela strålstyrningsområde.

Den andra 60 GHz-antennuppsättningen som utvecklats har en designad där en linjär ansluten kortplats med 16 lika stora punkter matas av en RFIC, Denna följs av en dielektrisk lins med hög förstärkning. De 16 matningarna kan styra huvudstrålen i azimutplanet när lämpliga vikter tillhandahålls. Strålstyrningsfunktionerna i designen har testats med fyra olika kraftdelare som kan styra helljuset vid 0°, 15°, 30° och 45°. Maximalt uppmätt förstärkning på 25,4 dBi har uppnåtts med denna design. Jag har visat att man med linsen kan uppnå jämförelsevis högre förstärkning när strålen styrs bort från dess bredd på grund av halvsfärisk avslutningar av linsen.

Två andra antennmatriser är utformade för att 28 GHz (**Publikation V, VI**) frekvensbandet med relativt lägre EIRP, Dessa lämpar sig för applikationer som kräver dataöverföring över längre sträckor. En linjärpolariserad och en cirkulärpolariserad grupp av antenner placeras i fläktområdet och bildar en

s.k. antenn-i-förpackningslösning (AiP). Den linjärpolariserade antennuppsättningen realiseras som en grupp dipolantenner som matar en hornformad kylfläns. Denna RF-modul ger en förstärkning på 34 dBm maximal EIRP med strålstyrning om ±35° i azimutplanet. Co- och korspolarisationsisoleringen är cirka 25 dB över hela frekvensbandet. Dessutom realiseras den cirkulära polariserade antennuppsättningen med hjälp av korsade dipoler vilket ger mindre än 3 dB axiellt förhållande 28 GHz frekvensbandet. RF-modulen ger 31 dBm maximal EIRP med strålstyrning om ±50°.

Den snabba utvecklingen av trådlös dataöverföring öppnar för nya möjligheter inom andra områden som t.ex. uppgraderingen av acceleratorer och experiment vid den stora hadronkollidern (LHC) vid CERN. Experimentet kommer att kräva betydligt högre dataöverföringskapacitet eftersom mängden data som genereras i experimenten ökar med en storleksordning. I detta arbete har jag undersökt genomförbarheten av 60 GHz trådlösa länkar för dataöverföring vid ett experiment på CERN (**Publikation II**). Till skillnad från de kommersiella trådlösa datanätverken kräver de som installeras i ett experiment på CERN mycket hög tålighet mot joniserande och partikelstrålning. Jag har därför bestrålat RFIC kretsar för 60 GHz trådlösa dataöverföring med 17 MeV-protoner till en dos av 7,4 Mrad (RX) och 4,2 Mrad (TX) samt med 200 MeV-elektroner till end dos av 270 Mrad (RX) och 314 Mrad (TX). Kretsarna har påverkats av strålningen men jag har visat att även efter bestrålningen kan de brukas med minimal prestandaförsämring efter proton- bestrålningen. Prestandasänkningen var mycket högre efter den dos som uppnåddes vid elektronbestrålningen. Studien visar att teknologin för trådlösa nätverk kan klara de krav som ställs för experiment vid CERN.

Acknowledgements

First and foremost, I express my gratitude to **Mirpur University of Science and Technology (MUST), Mirpur, Pakistan** for awarding the scholarship for this doctoral studies. And I am truly grateful to my supervisor **Dragos Dancila** who has given me this opportunity to pursue my studies in Sweden. He has significant contribution in the skills and knowledge I have acquired in the last four and a half years. Thank you Dragos for being always available and for your time to time push. Thank you for everything you have done for me.

I extend my deepest appreciation to my co-supervisors, **Richard Brenner** who has introduced and led me through the world of high energy physics and cryogenics. Thank you Richard. And thanks to **Anders Rydberg** for providing valuable feedback to my scientific works and also for your dedication and great contribution to the Microwave Group as always. I express my acknowledgements to **Tinus Stander** for reviewing my scientific work and for our technical discussions. And thanks to **Riana Geschke** for your valuable feedbacks.

A token of appreciation goes to **Anna Maria Lundin's scholarship foundation** as well for enabling me to attend an international conference along with couple of courses at world-class institutes in Europe.

I would take this chance to say thanks to my collaborators from Sivers IMA **Erik Öjefors**, **Johanna Hanning**, **Björn Franzen** and **Erik Wiklund**. You have significant role in my learning during this doctoral studies.

I express my gratitude to Microwave Group members **Long** and **Renbin**. Thank you for your availability whenever I needed. And thank you for your diverse discussions and lunch sittings. Wish you all the best in your career.

I like to convey my appreciation to **Jörgen Olsson** and **Uwe Zimmermann** for your lab facilities and equipment. Besides, thanks to Jörgen Olsson and **Roger Karlsson** for reviewing the scientific writings including papers and thesis. Thank you for your feedback. And I take this opportunity to thank my colleagues from the past to the present, **Ida, Syaiful, Jacob, Javad, Nishant, Robin, Mauricio, Corrado, Bappaditya, Pramod, Chenyu** and **Viktor** for adding the sweets and spices in my Ph.D. journey. Special thanks to Ida for being a nice neighbour.

Thank you **Ida Näslund, Linn Eriksson, Ramy Salameh** and **Ingrid Ringård** for taking care of the administrative matters and special thanks to **Jonatan Bagge** for your immediate help whenever asked.

Thank you **Omer Sher** for coffee breaks, and special thanks for developing my habit to walk. Thanks to **Hasan Ali, Ishtiaq Hassan Wani, Aqib Hayat** and **Muhammad Osama** for nice discussions, lively gatherings and your company. And special thanks to **Rana Iftikhar Ahmed** for welcoming me in Sweden and for your kitchen training.

At the end, I like to acknowledge my family. Thank you **Abu G** for your love, prayers and guidance. Thank you **Bhai jan, Baji, Qasmi** and **Kishwar** for your love and care. My final thanks goes to my dear wife, **Erum Shaheen**, my sweetest daughter **Amna Aziz** and little champ **Hamza Aziz** for your continuous moral and emotional support. I am very grateful to you Erum Shaheen for taking care of the family in my absence. I love you.

Imran Aziz
Uppsala, Sweden.
January 27, 2021.

References

[1] Cisco. Cisco annual internet report (2018–2023) white paper, March 9, 2020. `https://www.cisco.com/c/en/us/solutions/collateral/executive-perspectives/annual-internet-report/white-paper-c11-741490.html`.

[2] GSMA. Mobile internet connectivity 2019 global factsheet, 2019, Accessed on 2020-10-26. `https://www.gsma.com/mobilefordevelopment/wp-content/uploads/2019/07/Mobile-Internet-Connectivity-Global-Factsheet.pdf`.

[3] Statista. Global mobile data traffic from 2017 to 2022, 2020, Accessed on 2020-10-26. `https://www.statista.com/statistics/271405/global-mobile-data-traffic-forecast/#statisticContainer`.

[4] O. Semiari, W. Saad, M. Bennis, and M. Debbah. Performance Analysis of Integrated Sub-6 GHz-Millimeter Wave Wireless Local Area Networks. In *GLOBECOM 2017 - 2017 IEEE Global Communications Conference*, pages 1–7, 2017.

[5] Rohde Schwarz. 802.11ad - WLAN at 60 GHz A Technology Introduction, White Paper., 2017, Accessed on 2021-01-26. `https://scdn.rohde-schwarz.com/ur/pws/dl_downloads/dl_application/application_notes/1ma220/1MA220_3e_WLAN_11ad_WP.pdf`.

[6] GSMA. The WRC Series – 26 GHz and 28 GHz, Oct, 2019. Accessed on 2020-10-27. `https://www.gsma.com/spectrum/wp-content/uploads/2019/10/26-and-28-GHz-for-5G.pdf`.

[7] S. Dittmeier, N. Berger, A. Schöning, H.K. Soltveit, and D. Wiedner. 60 GHz wireless data transfer for tracker readout systems - First studies and results. *Journal of Instrumentation*, 9(11), 2014.

[8] R Brenner and S Cheng. Multigigabit wireless transfer of trigger data through millimetre wave technology. *Journal of Instrumentation*, 5(07):c07002–c07002, jul 2010.

[9] H K Soltveit, R Brenner, A Schöning, and D Wiedner. Multi-gigabit wireless data transfer at 60 GHz. *Journal of Instrumentation*, 7(12):C12016–C12016, Dec 2012.

[10] R. Brenner, S. Ceuterickx, C. Dehos, P. De Lurgio, Z. Djurcic, G. Drake, J. L. Gonzalez Gimenez, L. Gustafsson, D. W. Kim, E. Locci, D. Roehrich, A. Schoening, A. Siligaris, H. K. Soltveit, K. Ullaland, P. Vincent, D. Wiednert, and S. Yang. Development of Wireless Techniques in Data and Power Transmission - Application for Particle Physics Detectors. pages 1–20, 2015.

[11] Karolos Potamianos. The upgraded Pixel detector and the commissioning of the Inner Detector tracking of the ATLAS experiment for Run-2 at the Large Hadron Collider. In *The European Physical Society Conference on High Energy Physics*, 2016.

[12] S. Dittmeier, R. Brenner, D. Dancila, C. Dehos, P. De Lurgio, Z. Djurcic, G. Drake, J.L. Gonzalez Gimenez, L. Gustafsson, D.-W. Kim, E. Locci, U. Pfeiffer, D. Röhrich, A. Rydberg, A. Schöning, A. Siligaris, H.K. Soltveit, K. Ullaland, P. Vincent, P. Rodriguez Vazquez, D. Wiedner, and S. Yang. Wireless data transmission for high energy physics applications. *EPJ Web of Conferences*, 150:1–8, 2017.

[13] K. C. Huang and D. J Edwards. *Millimetre Wave Antennas for Gigabit Wireless Communications*, chapter 1, pages 1–36. John Wiley & Sons, Ltd, 2008.

[14] Zhouyue Pi and F. Khan. An introduction to millimeter-wave mobile broadband systems. *IEEE Communications Magazine*, 49, 2011.

[15] H. T. Friis. A note on a simple transmission formula. *Proceedings of the IRE*, 34(5):254–256, 1946.

[16] David J. Lockwood. *Rayleigh and Mie Scattering*, pages 1097–1107. Springer New York, 2016.

[17] everything RF. 60 GHz long range communication, Accessed on 2020-10-07. https://www.everythingrf.com/community/why-is-the-60-ghz-band-not-good-for-long-range-communications.

[18] G.A. Deschamps. Microstrip Microwave Antennas. *3rd USAF Symposium on Antennas*, 1953.

[19] Ali Daliri, Amir Galehdar, Wayne S. T. Rowe, Sabu John, Chun H. Wang, and Kamran Ghorbani. Quality Factor Effect on the Wireless Range of Microstrip Patch Antenna Strain Sensors. *Sensors*, 14(1):595–605, 2014.

[20] P. Agrawal and M. Bailey. An analysis technique for microstrip antennas. *IEEE Transactions on Antennas and Propagation*, 25(6):756–759, 1977.

[21] Y. Lo, D. Solomon, and W. Richards. Theory and experiment on microstrip antennas. *IEEE Transactions on Antennas and Propagation*, 27(2):137–145, 1979.

[22] W. Richards, Yuen Lo, and D. Harrison. An improved theory for microstrip antennas and applications. *IEEE Transactions on Antennas and Propagation*, 29(1):38–46, 1981.

[23] D. M. Pozar. Microstrip antennas. *Proceedings of the IEEE*, 80(1):79–91, 1992.

[24] Constantine A Balanis. *Antenna theory: analysis and design*. John wiley & sons, 2016.

[25] Jaco du Preez and Saurab Sinha. Millimeter-Wave Antennas: Configurations and Applications. chapter 3. Springer International Publishing Switzerland, 2016.

[26] D. M. Pozar and D. H. Schaubert. *Microstrip Antennas: The Analysis and Design of Microstrip Antennas and Arrays*. Wiley-IEEE Press, 1995.

[27] J. R. James and P. S. Hall. *Handbook of Microstrip Antennas*, volume 1, chapter 3. Peter Peregrinus Ltd. UK on behalf of the Institution of Electrical Engineers, 1989.

[28] Randy Bancroft. Microstrip and Printed Antenna Design (2nd Edition). chapter 4. SciTech Publishing, 2009.

[29] Tao Zhang, Lianming Li, Haiyang Xia, Xujun Ma, and Tie Jun Cui Cui. A Low-Cost and High-Gain 60-GHz Differential Phased Array Antenna in PCB Process. *IEEE Transactions on Components, Packaging and Manufacturing Technology*, 8(7):1281–1291, 2018.

[30] R. Wang, B. Wang, X. Ding, and X. Yang. Planar phased array with wide-angle scanning performance based on image theory. *IEEE Transactions on Antennas*

and Propagation, 63(9):3908–3917, 2015.

[31] S. E. Valavan, D. Tran, A. G. Yarovoy, and A. G. Roederer. Dual-band wide-angle scanning planar phased array in x/ku-bands. *IEEE Transactions on Antennas and Propagation*, 62(5):2514–2521, 2014.

[32] S. E. Valavan, D. Tran, A. G. Yarovoy, and A. G. Roederer. Planar dual-band wide-scan phased array in x-band. *IEEE Transactions on Antennas and Propagation*, 62(10):5370–5375, 2014.

[33] R. Wang, B. Wang, C. Hu, and X. Ding. Wide-angle scanning planar array with quasi-hemispherical-pattern elements. *Scientific Reports*, 7, 2017.

[34] Y. Wen, B. Wang, and X. Ding. A wide-angle scanning and low sidelobe level microstrip phased array based on genetic algorithm optimization. *IEEE Transactions on Antennas and Propagation*, 64(2):805–810, 2016.

[35] H. J. Visser. *Array and Phased Array Antenna Basics*, chapter 4, The Linear Broadside Array Antenna, pages 123–135. John Wiley Sons, Ltd, 2005.

[36] E. Öjefors, M. Andreasson, T. Kjellberg, H. Berg, L. Aspemyr, R. Nilsson, K. Brink, R. Dahlbäck, D. Wu, K. Sjögren, and M. Carlsson. A 57-71 GHz Beamforming SiGe Transceiver for 802.11 ad-Based Fixed Wireless Access. In *2018 IEEE Radio Frequency Integrated Circuits Symposium (RFIC)*, pages 276–279, 2018.

[37] I. Uchendu and J. R. Kelly. Survey of beam steering techniques available for millimeter wave applications. *Progress In Electromagnetics Research B*, 68(5):35–54, 2016.

[38] Tomohiro Seki, Naoki Honma, Kenjiro Nishikawa, and Kouichi Tsunekawa. A 60-GHz multilayer parasitic microstrip array antenna on LTCC substrate for system-on-package. *IEEE Microwave and Wireless Components Letters*, 15(5):339–341, 2005.

[39] Tomohiro Seki, Kenjiro Nishikawa, and Kazuyasu Okada. 60-GHz multi-layer parasitic microstrip array antenna with stacked rings using multi-layer LTCC substrate. *2008 IEEE Radio and Wireless Symposium, RWS*, pages 679–682, 2008.

[40] Alexander Bondarik, Dong Jun Suk, Joung Kim Myoun, and Je Yun Hoon. Investigation of Microstrip Antenna Array Stacked Struture Realized on LTCC for 60 GHz Band. *Microwave and Optical Technology Letters*, 52(3):648–652, 2010.

[41] Wonbin Hong, Alexander Goudelev, Kwang Hyun Baek, Vladimir Arkhipenkov, and Juhyung Lee. 24-element antenna-in-package for stationary 60-GHz Communication scenarios. *IEEE Antennas and Wireless Propagation Letters*, 10:738–741, 2011.

[42] Zhi Ning Chen, Xianming Qing, Mei Sun, Ke Gong, and Wei Hong. 60-GHz antennas on PCB. *8th European Conference on Antennas and Propagation, EuCAP 2014*, (EuCAP):533–536, 2014.

[43] Oleksandr Vasylchenko. *Towards the miniaturization of new ultra wideband small integrated antenna topologies*. PhD thesis, Katholieke Universiteit Leuven, September 2010.

[44] Alexey Artemenko, Alexander Maltsev, Andrey Mozharovskiy, Alexey Sevastyanov, Vladimir Ssorin, and Roman Maslennikov. Millimeter-wave electronically steerable integrated lens antennas for WLAN/WPAN applications. *IEEE Transactions on Antennas and Propagation*, 61(4):1665–1671, 2013.

[45] J. Ala-Laurinaho, A. Karttunen, J. Säily, A. Lamminen, R. Sauleau, and A. Räisänen. MM-wave lens antenna with an integrated LTCC feed array for beam steering. *Antennas and Propagation (EuCAP), 2010 Proceedings*, pages 1–5, 2010.

[46] A Karttunen, J Ala-Laurinaho, R Sauleau, and A V Raisanen. A study of extended hemispherical lenses for a high-gain beam-steering antenna. *Antennas and Propagation (EuCAP), 2010 Proceedings of the Fourth European Conference on*, (2):1–5, 2010.

[47] Xidong Wu, George V. Eleftheriades, and T. Emilie Van Deventer-Perkins. Design and characterization of single- and multiple-beam MM-wave circularly polarized substrate lens antennas for wireless communications. *IEEE Transactions on Microwave Theory and Techniques*, 49(3):431–441, 2001.

[48] Daniel F. Filipovic, Gildas P. Gauthier, Sanjay Raman, and Gabriel M. Rebeiz. Off-axis properties of silicon and quartz dielectric lens antennas. *IEEE Transactions on Antennas and Propagation*, 45(5):760–766, 1997.

[49] Antti Lamminen. *Design of millimetre-wave antennas on LTCC and PCB technologies for beam-steering applications*. PhD thesis, Aalto University publication series Doctoral dissertations; 194/2019, 2019.

[50] NXP. AN10439 application note: Wafer-level chip-scale package (fan-in WLP and fan-out WLP), July 2018. Accessed on 2021-01-21. `https://www.nxp.com/docs/en/application-note/AN10439.pdf`.

[51] R. Hsieh, F. Chu, C. Ho, and C. Wang. Advanced Thin-Profile Fan-Out with Beamforming Verification for 5G Wideband Antenna. In *2019 IEEE 69th Electronic Components and Technology Conference (ECTC)*, pages 977–982, 2019.

[52] S. Hsieh, F. Chu, C. Ho, and C. Wang. mm-Wave Antenna Design in Advanced Fan-Out Technology for 5G Application. In *2019 22nd European Microelectronics and Packaging Conference Exhibition (EMPC)*, pages 1–4, 2019.

[53] C. Tsai, J. Hsieh, M. Liu, E. Yeh, H. Chen, C. Hsiao, C. Chen, C. Liu, M. Lii, C. Wang, and D. Yu. Array antenna integrated fan-out wafer level packaging (InFO-WLP) for millimeter wave system applications. In *2013 IEEE International Electron Devices Meeting*, pages 25.1.1–25.1.4, 2013.

[54] Z. Chen, L. T. Guan, D. S. Wee Ho, and S. Bhattacharya. Millimeter-Wave Antenna in Fan-Out Wafer Level Packaging for 60 GHz WLAN Application. In *2018 IEEE 68th Electronic Components and Technology Conference (ECTC)*, pages 331–336, 2018.

[55] F. Ahmed, M. Furqan, and A. Stelzer. On the Design of Antennas in eWLB Package for Radar Applications above 100 GHz. In *2019 IEEE MTT-S International Microwave Workshop Series on Advanced Materials and Processes for RF and THz Applications (IMWS-AMP)*, pages 145–147, 2019.

[56] I. Nasr, R. Jungmaier, A. Baheti, D. Noppeney, J. S. Bal, M. Wojnowski, E. Karagozler, H. Raja, J. Lien, I. Poupyrev, and S. Trotta. A Highly Integrated 60 GHz 6-Channel Transceiver With Antenna in Package for Smart Sensing and Short-Range Communications. *IEEE Journal of Solid-State Circuits*, 51(9):2066–2076, 2016.

[57] A. Fischer, Z. Tong, A. Hamidipour, L. Maurer, and A. Stelzer. 77-GHz Multi-Channel Radar Transceiver With Antenna in Package. *IEEE Transactions on Antennas and Propagation*, 62(3):1386–1394, 2014.

[58] T. H. Le, A. Kanitkar, M. Rossi, I. Ndip, T. Braun, F. Mueller, K. D. Lang,

M. Wieland, C. Goetze, S. B. Halim, and J. Trewhella. Dual-Band 5G Antenna Array in Fan-Out Wafer-Level Packaging (FOWLP) Technology. In *2020 23rd International Microwave and Radar Conference (MIKON)*, pages 157–161, 2020.

[59] G. Huang, Y. Dai, N. Liu, Z. Duan, Y. Wu, and T. Lin. A low cost 60GHz antenna in Fan-Out Panel Level Package for millimeter-wave radar application. In *2020 21st International Conference on Electronic Packaging Technology (ICEPT)*, pages 1–4, 2020.

[60] A. Fischer, Z. Tong, A. Hamidipour, L. Maurer, and A. Stelzer. A 77-GHz antenna in package. In *2011 8th European Radar Conference*, pages 428–431, 2011.

[61] Z. Chen, X. Zhu, and L. Zhong. Multi-port power combining grid array antenna on fan-out wafer level packaging. In *2020 IEEE MTT-S International Microwave Workshop Series on Advanced Materials and Processes for RF and THz Applications (IMWS-AMP)*, pages 1–3, 2020.

[62] C. Ho, S. Hsieh, M. Jhong, H. Kuo, C. Ting, and C. Wang. A Low-Cost Antenna-in-Package Solution for 77GHz Automotive Radar Applications. In *2019 International Conference on Electronics Packaging (ICEP)*, pages 110–114, 2019.

[63] M. PourMousavi, M. Wojnowski, R. Agethen, R. Weigel, and A. Hagelauer. Antenna array in eWLB for 61 GHz FMCW radar. In *2013 Asia-Pacific Microwave Conference Proceedings (APMC)*, pages 310–312, 2013.

[64] D. Wu, R. Dahlbäck, E. Öjefors, M. Carlsson, F. C. P. Lim, Y. K. Lim, A. K. Oo, W. K. Choi, and S. W. Yoon. Advanced Wafer Level PKG Solutions for 60GHz WiGig (802.11ad) Telecom Infrastructure. In *2019 IEEE 69th Electronic Components and Technology Conference (ECTC)*, pages 968–971, 2019.

[65] B. Li, Y. Yin, W. Hu, Y. Ding, and Y. Zhao. Wideband dual-polarized patch antenna with low cross polarization and high isolation. *IEEE Antennas and Wireless Propagation Letters*, 11:427–430, 2012.

[66] J. Perruisseau-Carrier, T. W. Hee, and P. S. Hall. Dual-polarized broadband dipole. *IEEE Antennas and Wireless Propagation Letters*, 2:310–312, 2003.

[67] H. D. Hristov, H. Carrasco, R. Feick, and B. L. Ooi. Low-profile x antenna with flat reflector for polarization diversity applications. *Microwave and Optical Technology Letters*, 51(6):1508–1512, 2009.

[68] F. Leon Lerma, G. Ruvio, and M. J. Ammann. A microstrip-fed printed crossed dipole for wireless applications. *Microwave and Optical Technology Letters*, 48(4):751–753, 2006.

[69] M. F. Bolster. A new type of circular polarizer using crossed dipoles. *IRE Transactions on Microwave Theory and Techniques*, 9(5):385–388, 1961.

[70] OML Inc. VNA extension modules, Accessed on 2021-01-21. `https://www.omlinc.com/products/vna-extension-modules`.

[71] H. J. Visser. *Array and Phased Array Antenna Basics*, chapter 7, The Linear Phased Array Antenna, pages 201–219. John Wiley Sons, Ltd, 2005.

[72] B. Ahn, I. Hwang, K. Kim, S. Chae, J. Yu, and H. Lee. Wide-angle scanning phased array antenna using high gain pattern reconfigurable antenna elements. *Scientific Reports*, 9, 2019.

[73] M. Huhtinen. Simulation of non-ionising energy loss and defect formation in silicon. *Nuclear Instruments and Methods in Physics Research Section A: Ac-*

celerators, Spectrometers, Detectors and Associated Equipment, 491:194–215, 2002.

[74] Frank Hönniger. *Radiation damage in silicon: Defect analysis and detector properties*. PhD thesis, Hamburg University, 2007.

[75] Y. Shi, D. X. Shen, F. M. Wu, and K. J. Cheng. A numerical study of cluster center formation in neutron-irradiated silicon. *Journal of Applied Physics*, 67(2):1116–1118, 1990.

[76] J. R. Schwank. Basic mechanisms of radiation effects in the natural space radiation environment. In *31st Annual International Nuclear and Space Radiation Effects Conference*, pages 18–22, January 1994.

[77] T. R. Oldham. Analysis of Damage in MOS Devices for Several Radiation Environments. *IEEE Transactions on Nuclear Science*, 31(6):1236–1241, 1984.

[78] J. R. Srour. Basic mechanisms of radiation effects on electronic materials, devices, and integrated circuits. In *IEEE NSREC 1983*, 1983.

[79] F. B. McLean and T. R. Oldham. Basic mechanisms of radiation effects in electronic materials and devices. Final report. September 1987. `https://www.osti.gov/biblio/5646360` (Accessed on 2021-01-25).

[80] Stefano Meroli. Radiation damage for silicon wafers, Accessed on 2021-01-31. `https://meroli.web.cern.ch/lecture_radiation_damage_silicon_detector.html`.

[81] Investigation of total ionizing dose effect and displacement damage in 65nm CMOS transistors exposed to 3MeV protons. *Nuclear Instruments and Methods in Physics Research Section A*.

[82] F. Faccio and G. Cervelli. Radiation-induced edge effects in deep submicron CMOS transistors. *IEEE Transactions on Nuclear Science*, 52(6):2413–2420, 2005.

Acta Universitatis Upsaliensis

Digital Comprehensive Summaries of Uppsala Dissertations from the Faculty of Science and Technology 2005

Editor: The Dean of the Faculty of Science and Technology

ACTA
UNIVERSITATIS
UPSALIENSIS
UPPSALA
2021